

Search for Cosmological time dilation from Gamma-Ray Bursts - A 2021 status update

Amitesh Singh^{1*} and Shantanu Desai^{2†}

¹ *University of Mississippi, University, MS, USA-38677 and*

² *Indian Institute of Technology, Hyderabad, Kandi, Telangana, India*

(Dated: January 25, 2022)

We carry out a search for signatures of cosmological time dilation in the light curves of Gamma Ray Bursts (GRBs), detected by the Neil Gehrels Swift Observatory. For this purpose, we calculate two different durations (T_{50} and T_{90}) for a sample of 247 GRBs in the fixed rest frame energy interval of 140-350 keV, similar to a previous work [1]. We then carry out a power law-based regression analysis between the durations and redshifts. This search is done using both the unbinned as well as the binned data, where both the weighted mean and the geometric mean was used. For each analysis, we also calculate the intrinsic scatter to determine the tightness of the relation. We find that the weighted mean-based binned data for long GRBs and the geometric mean-based binned data is consistent with the cosmological time dilation signature, whereas the analyses using unbinned durations show a very large scatter. We also make our analysis codes and the procedure for obtaining the light curves and estimation of T_{50}/T_{90} publicly available.

I. INTRODUCTION

Gamma-ray bursts (GRBs) are short-duration single-shot transient events detected in keV-MeV energy range, and constitute one of the biggest and brightest explosions in the universe, with isotropic-equivalent energies between 10^{48} and 10^{55} ergs [2]. GRBs have been traditionally bifurcated into two categories based on T_{90} and T_{50} , which represent the durations over which 90% and 50% of fluence are detected, respectively [3]. GRBs with $T_{90} > 2$ secs are known as long bursts and associated with core-collapse supernovae, whereas those with $T_{90} < 2$ seconds are known as short bursts and usually associated with compact object mergers [4–7]. There are, however, exceptions to this broad dichotomy, and additional sub-classes of GRBs have also been identified [8–17]. The smoking gun evidence for the association of short GRBs with compact binary object mergers (involving neutron stars) was, however, provided by the simultaneous detection of gravitational waves and gamma rays from GW170817/GRB170817A [18], which also enabled tests of a whole slew of modified gravity theories [19].

Although GRBs were first detected in the 1970s [20] there were still lingering doubts as to whether GRBs are local or cosmological until the 1990s (see the contrasting viewpoints on this issue by [21] versus [22], as of 1995.) This issue was unequivocally resolved in favour of a cosmological origin, after the first precise localization and redshift determination in 1997 from the Beppo-Sax satellite [23]. After the launch of the Neil Gehrels Swift observatory (Swift, hereafter), a large number of GRBs with confirmed redshifts have been detected [24].

Despite this, no smoking gun signature of cosmological time dilation has emerged in the GRB light curves ever since the earliest proposed attempts [25, 26], unlike the corresponding signature found in Type Ia supernovae [27]. We note, however, that such a time dilation has also not been seen in quasar light curves, although the reasons have been attributed to other astrophysical effects which mask the cosmological time dilation signal [28]. Before the launch of the Swift satellite, there were a few indirect pieces of evidence for cosmological time dilation in GRB light curves [29–33]. The main difficulty in coming to a robust conclusion in these early studies stemmed from the uncertainty in the intrinsic GRB duration and very little statistics of GRBs with well-measured redshifts. However, even after the launch of Swift and FERMI gamma-ray space telescope, there were no smoking gun signatures of cosmological time dilation in the GRB light curves [34–38] or via indirect methods such as through the skewness of T_{90} distributions [39].

The first novel attempt at measuring a robust signature of cosmological time dilation using a large sample of Swift GRBs was carried out by Zhang et al. [1] (Z13, hereafter). Z13 pointed out that all previous studies of cosmological time dilation prior to their work were carried out from the durations in the observer frame using a fixed energy interval, usually corresponding to the energy sensitivity of the detector, which was the main reason for not seeing a smoking-gun signature. To circumvent this, they calculated the durations for a sample of 139 Swift GRBs using a fixed energy interval between 140-350 keV in the GRB rest frame, followed by calculating the observed durations using $E_{obs} = E_{rest}/(1+z)$, where E_{obs} and E_{rest} denote the photon energy in the observer and rest frame, respectively.

*asingh10@go.olemiss.edu

†shntn05@gmail.com

Z13 showed after binning the data as a function of redshift that the durations were correlated with $(1+z)$, i.e., $(T_{90} \propto (1+z)^{0.94 \pm 0.26})$. This analysis was then extended by [40] to 237 Swift GRBs and 57 Fermi-GBM GRBs using three independent measures of duration: T_{90} , T_{50} , and T_{R45} . They showed that the binned data for the Swift GRB sample is broadly consistent with cosmological time dilation.

We independently carry out the same procedure as Z13 by using the latest Swift GRB database. We then carry out a power-law based regression analysis between the durations and redshifts using both the unbinned well as binned data. We also thoroughly document the procedure for obtaining the Swift light curves for every GRB and obtain the T_{90} , which would benefit readers for carrying out any analysis using the GRB light curves. This manuscript is organized as follows. Our data analysis and results are presented in Sect. II. We conclude in Sect. III. Detailed documentation of the procedure to get the GRB light curves and calculate T_{50}/T_{90} can be found in Appendix A.

II. DATA ANALYSIS AND RESULTS

We construct light curves for all the GRBs detected by Swift with confirmed redshifts in the fixed rest frame energy interval between 140-350 keV (similar to Z13), and thereby determine T_{50} and T_{90} . The full step-by-step procedure to download these light curves and obtain T_{50}/T_{90} is documented in Appendix A. We have also uploaded these codes on a `github` link, which can be found at the end of the manuscript. Out of all the GRBs containing redshift data present in the Swift database (around 400), we were able to determine the durations for 247 of them. A tabulated summary of these durations along with 1σ rs in the fixed rest frame energy interval (140-350 keV) as well as the full energy range in the observer frame for all GRBs can be found in Table III.

We now describe the procedure for checking if the aforementioned GRB durations are consistent with the signature of cosmological time dilation. For this purpose, we carry out a power law-based regression analysis between the observed durations and the redshift using the following equation

$$y = Ax^B \quad (1)$$

where A and B are parameters of our model (unknown before the analysis, x is an input variable with $x = (1+z)$, where z is the redshift, and y denotes the burst interval (either T_{90} or T_{50}) in seconds. For cosmological time dilation, B should be equal to one.

To get the best-fit parameters we maximize the likelihood as follows:

$$\begin{aligned} -2 \ln L &= \sum_i \ln 2\pi\sigma_i^2 + \sum_i \frac{[y_i - Ax_i^B]^2}{\sigma_i^2} \\ \sigma_i^2 &= \sigma_{y_i}^2 + m^2\sigma_{x_i}^2 + \sigma_{int}^2 \end{aligned} \quad (2)$$

where x_i is $(1+z)$ data for every GRB. Similar to our works on galaxy clusters [41–43] and also [44], we have added in quadrature, an unknown intrinsic scatter σ_{int} as an additional free parameter while fitting for Eq. 1. This can be used to parameterize the tightness of the scatter in the relation. A value of $\sigma_{int} > 1$ indicates that the relation has a lot of scatter and that any relation between the two variables cannot be discerned. On the other hand, a small value of scatter points to a deterministic relation between the two variables. Note that Z13 have investigated for putative correlations between the durations and redshifts using the Pearson correlation coefficient. However, the Pearson correlation coefficient does not take into account the errors in the observables. The magnitude of the intrinsic scatter would be a more robust diagnostic of the scatter.

We use the `emcee` MCMC routine [45] to sample the above likelihood and obtained 68%, 90%, and 95% marginalized credible intervals on each of the parameters. We use uniform priors on all the free parameters : $0 < A < 50$, $-1 < B < 4$, $-5 < \ln(\sigma_{int}) < 5$. In all the cases, the marginalized contours were obtained using the `Corner` package, and estimates are performed over parameters of the model which we are trying to optimize.

We now present our results. We carried out multiple analyses for both T_{50} and T_{90} , using both the unbinned data as well as using the binned data. The binning was done in equal-sized redshift bins and with two different ways of averaging the data in each bin: viz. weighted mean (as in Z13) and the geometric mean (as in [40]). Our results are summarized in Table I and II.

• Analysis using unbinned data for all GRBs

We first fit the T_{50} and T_{90} obtained for all the 247 GRBs in our sample to Eq. 1. The marginalized credible intervals for the unbinned data are given by Fig. 1 and Fig. 2 for both T_{50} and T_{90} , respectively. As we can see, the intrinsic scatter is greater than 100%, indicating that it is difficult to discern a deterministic relation between T_{50} or T_{90} and the redshift. Furthermore, the power-law index B is not equal to the cosmological

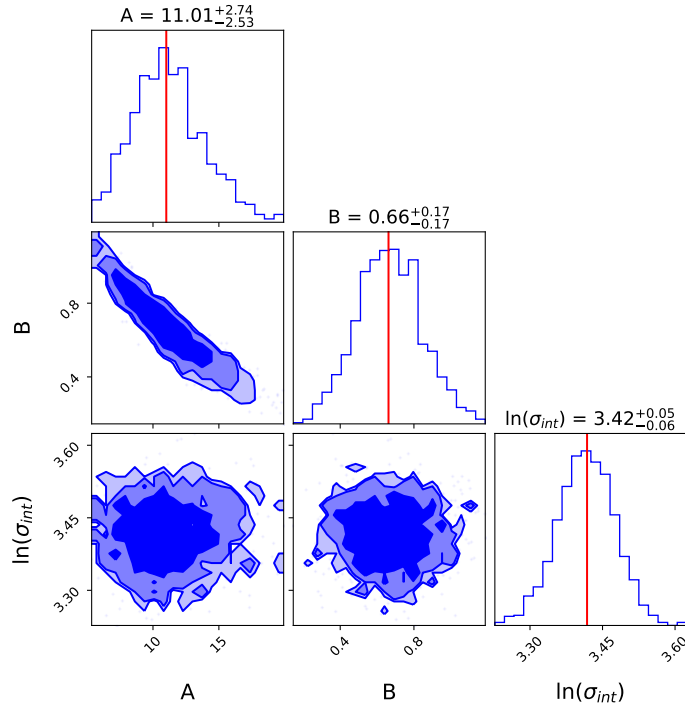


FIG. 1: Figure showing the contour plot for T_{50} in the rest-frame energy range 140-350 keV, for the unbinned GRB data. The contours represent 68%, 90%, and 95% credible intervals. As we can see, the intrinsic scatter is quite high ($> 100\%$), which implies that it is hard to discern a deterministic relation between T_{50} and the redshift.

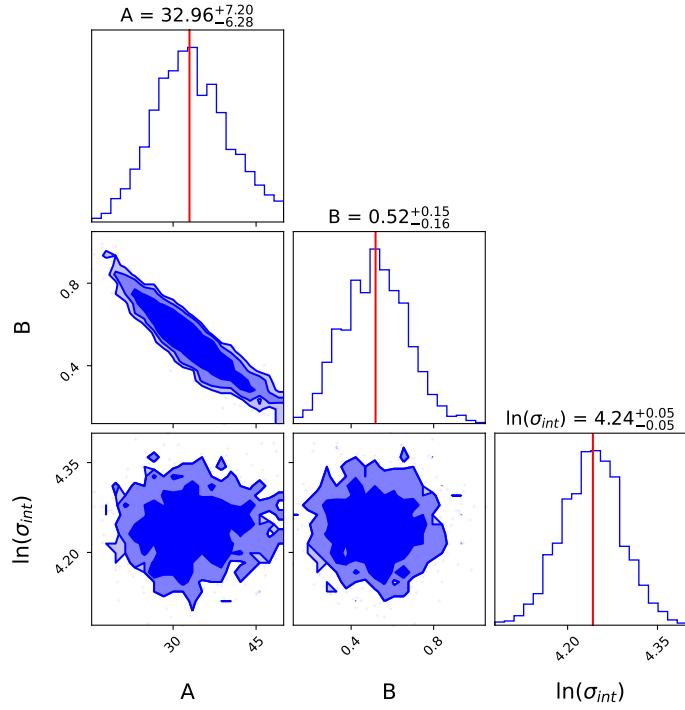


FIG. 2: Figure showing the contour plot T_{90} in the rest-frame energy range 140-350 keV, for the unbinned GRB data. The contours represent 68%, 90%, and 95% credible intervals. Again, the intrinsic scatter is very high ($> 100\%$).

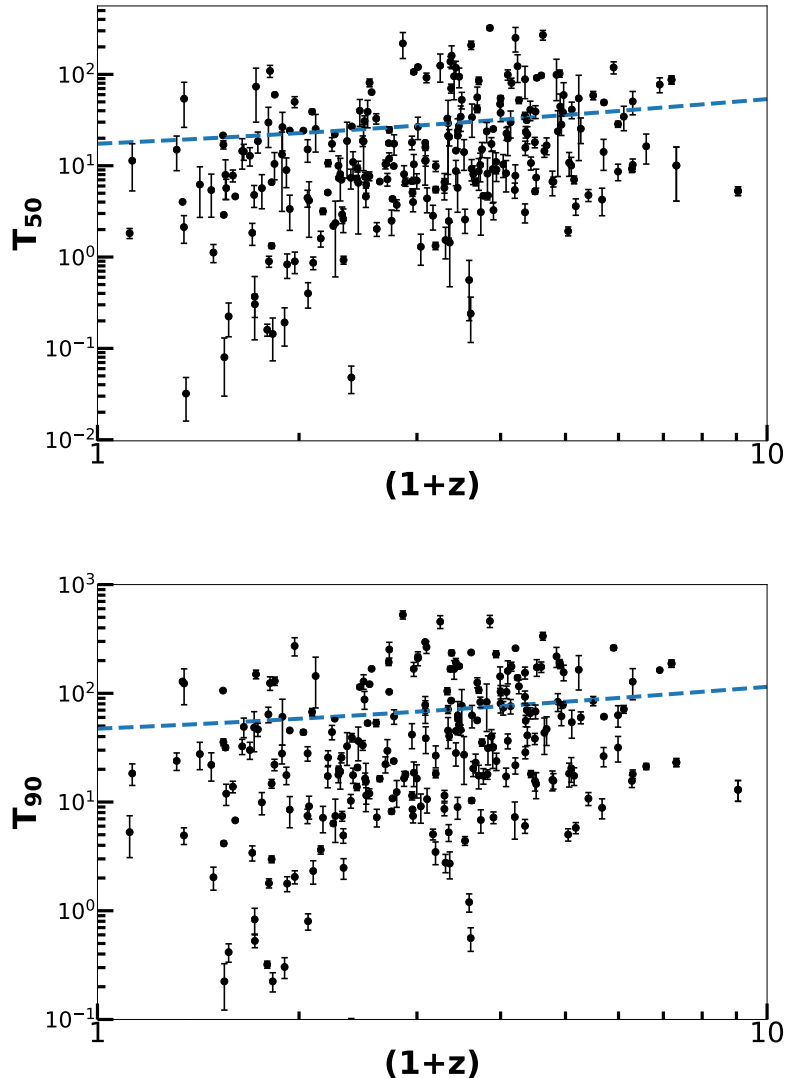


FIG. 3: Figure showing the relationship between the burst intervals, T_{90} and T_{50} in the observer frame energy range $E_1 = 140/(1+z)$ keV and $E_2 = 350/(1+z)$ keV (denoted by T_{90} , T_{50}), for the unbinned GRB data. The data points have been plotted with their respective error bars. The best fits are shown by the dashed blue lines and those are $T_{50} = 11.01(1+z)^{0.66}$ and $T_{90} = 32.96(1+z)^{0.52}$ respectively.

expected value of one to within 1σ . Fig. 3 shows the plots for both the burst intervals, T_{90} and T_{50} , along with the best-fit obtained from fitting the full unbinned data.

- **Analysis using weighted-mean binned data for all GRBs**

We now re-analyze this data by binning the data into six bins with equal redshift intervals and using the error-weighted means of both the burst intervals, T_{90} and T_{50} in each redshift bin. The marginalized contours for A and B for such a binned analysis for both T_{50} and T_{90} can be found in Figs. 4 and 5, respectively. We find that B is discrepant from the cosmological expected value of one at 1.2σ (T_{50}) and 2σ (T_{90}). The intrinsic scatters are approximately 75% for both T_{50} and T_{90} . This shows that there is still no evidence for cosmological time dilation signature using the complete binned sample. The binned data along with the best fit can be found in Fig. 6.

- **Analysis using unbinned data for long GRBs**

Z13 and Ref. [40] did their analysis using only long GRBs, with $T_{90} > 2$ secs. The reason for this exclusion of

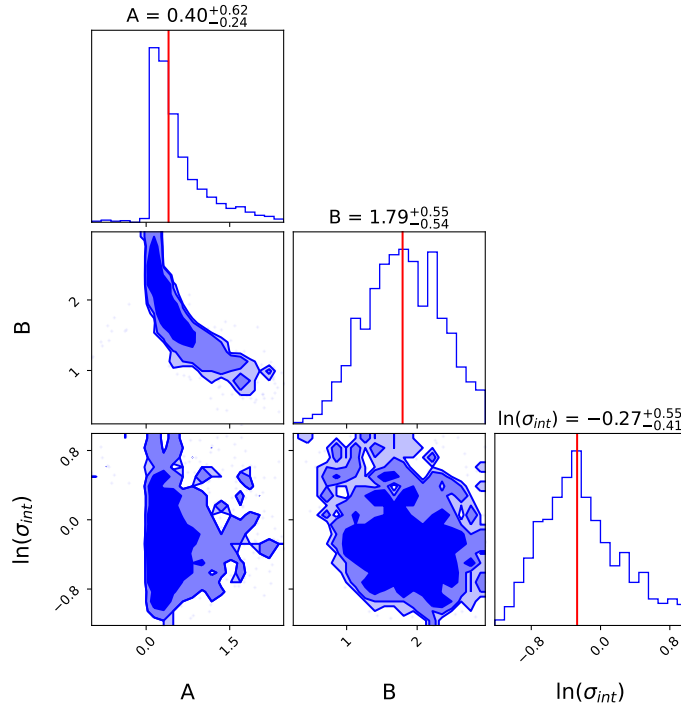


FIG. 4: Contours for A and B for T_{50} in the rest-frame energy range 140-350 keV. The input data is the weighted mean of binned data of T_{50} vs the binned redshifts $(1+z)$. This data is then fit to Eq 1. We have shown 68%, 90%, and 95% credible intervals. The intrinsic scatter we obtain is about 76%. The value of B is discrepant with the signature of cosmological time dilation at about 1.2σ .

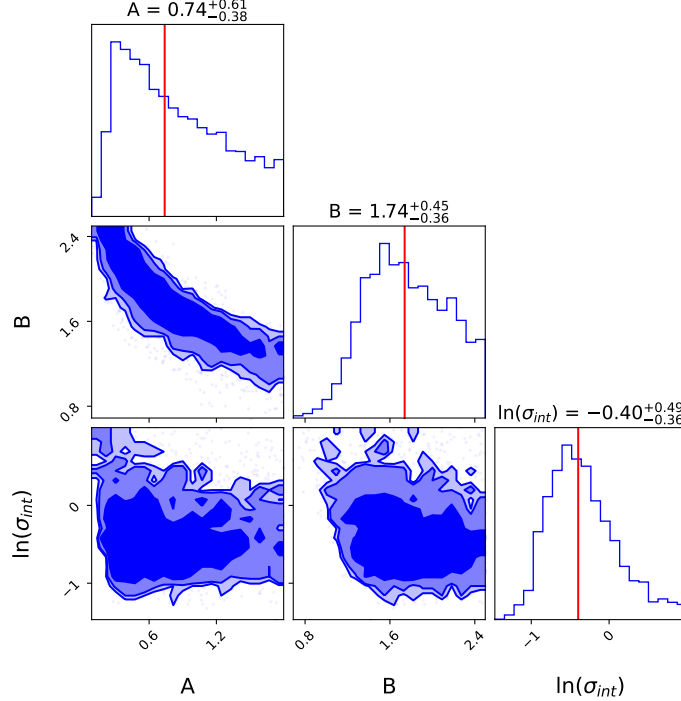


FIG. 5: Contours for A and B using 90% burst interval, T_{90} in the rest-frame energy range 140-350 keV. Input data is the weighted mean of binned data of the T_{90} vs the binned redshifts $(1+z)$. This data is then fit to Eq. 1. We have shown 68%, 90%, and 95% credible intervals. The intrinsic scatter is equal to 76.3%. The value of B is discrepant with the signature of cosmological time dilation at about 2σ .

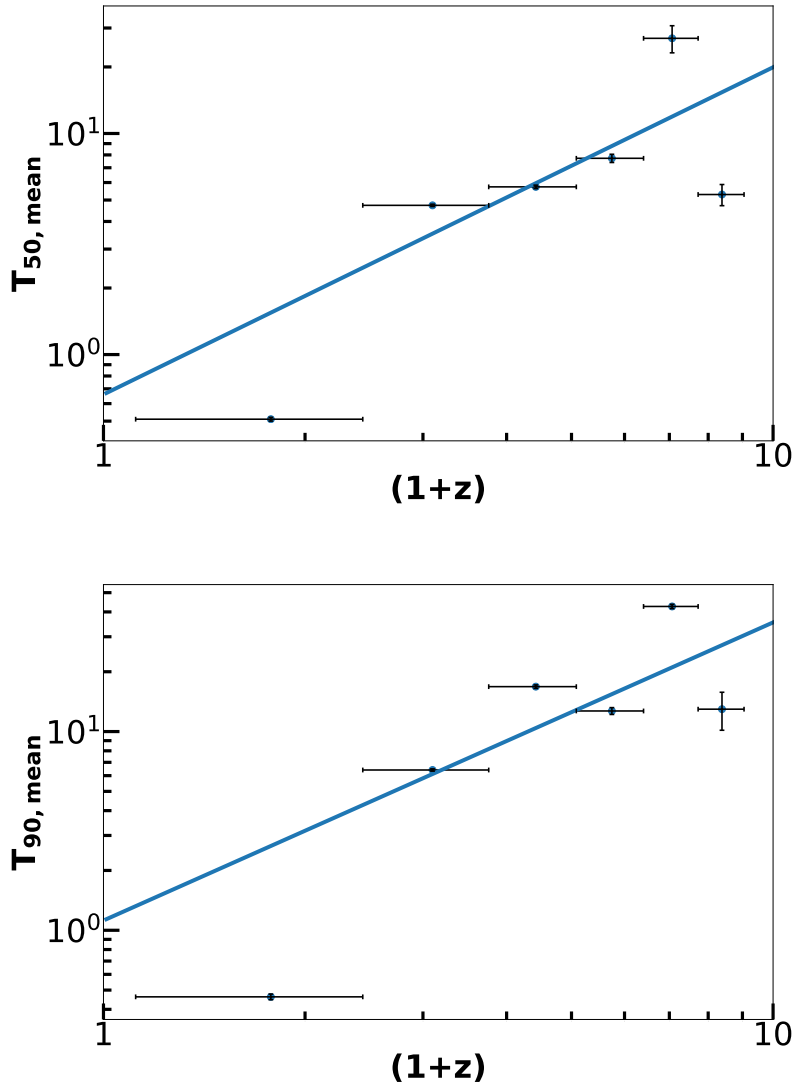


FIG. 6: Plots showing the weighted means of the burst intervals with the binned redshift data (containing 6 groups equally spaced in z), where the horizontal errors bars denote the redshift range in each group. The blue line curve is our best fit for the data obtained through the estimation of parameters A and B . The best-fits shown are $T_{50} = 0.40(1+z)^{1.79}$ and $T_{90} = 0.74(1+z)^{1.74}$.

short GRBs is to have a pure sample with an intrinsically similar distribution. We now present similar results using only long GRBs with the cut of $T_{90,raw} > 2$ secs. We show the marginalized contours for both A and B , for both T_{90} and T_{50} in Figs. 7 and 8. Similar to the full unbinned GRB dataset, the intrinsic scatter is $> 100\%$ making it impossible to discern any relation between the duration and redshift. Furthermore, the values of B are not equal to one (at more than 1σ) for both T_{90} and T_{50} Fig. 9 shows the burst intervals as a function of redshift for this subset along with the best fit.

- **Analysis using binned data for long GRBs**

We now bin the data for long GRBs and use the weighted mean in each redshift bin. The marginalized contours for both A and B , which are obtained by fitting the model in Eq. 1, using the binned data can be found in Figs 10 and 11. We obtain intrinsic scatters of 57% and 55% for T_{50} and T_{90} , respectively. The values of B for both the binned durations are consistent with the cosmological time dilation signature ($B = 1$) to within 1σ . We show the weighted mean burst intervals for these long GRBs, with redshifts in Fig. 12, along with the best-fit.

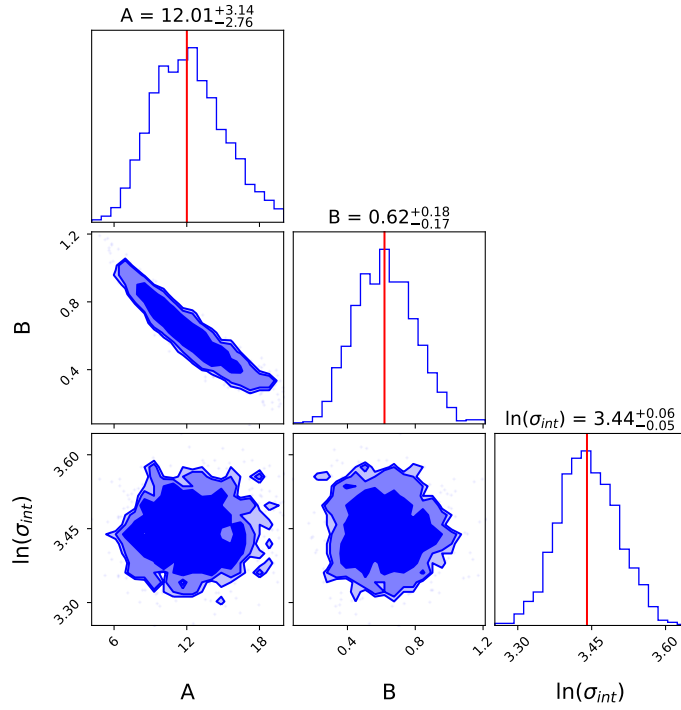


FIG. 7: Contours for A and B for T_{50} , in the rest-frame energy range 140-350 keV for long GRBs which have $T_{90,raw}$ greater than 2 secs. We have shown 68%, 90%, and 95% credible intervals. The intrinsic scatter is greater than 100%.

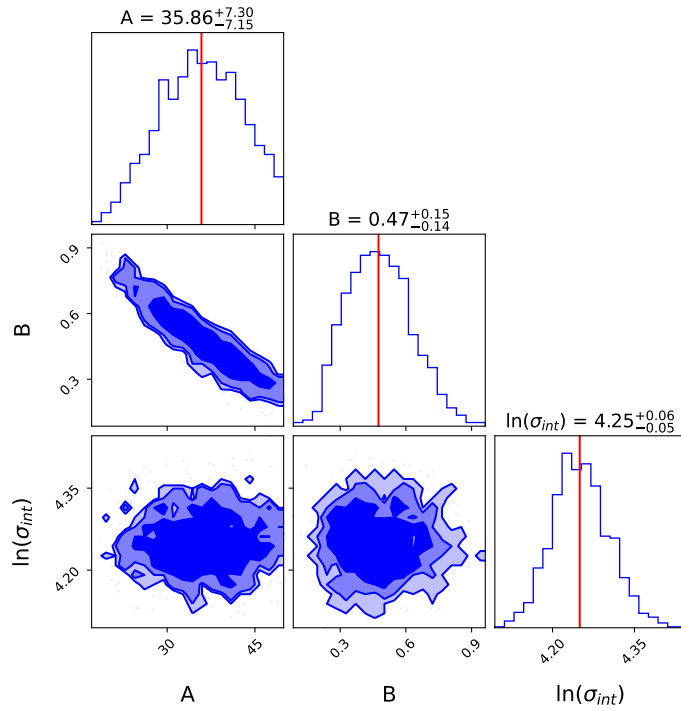


FIG. 8: Contours for A and B for T_{90} in the rest-frame energy range 140-350 keV, for long GRBs which had a $T_{90,raw}$ greater than 2 secs. The intrinsic scatter is greater than 100%.

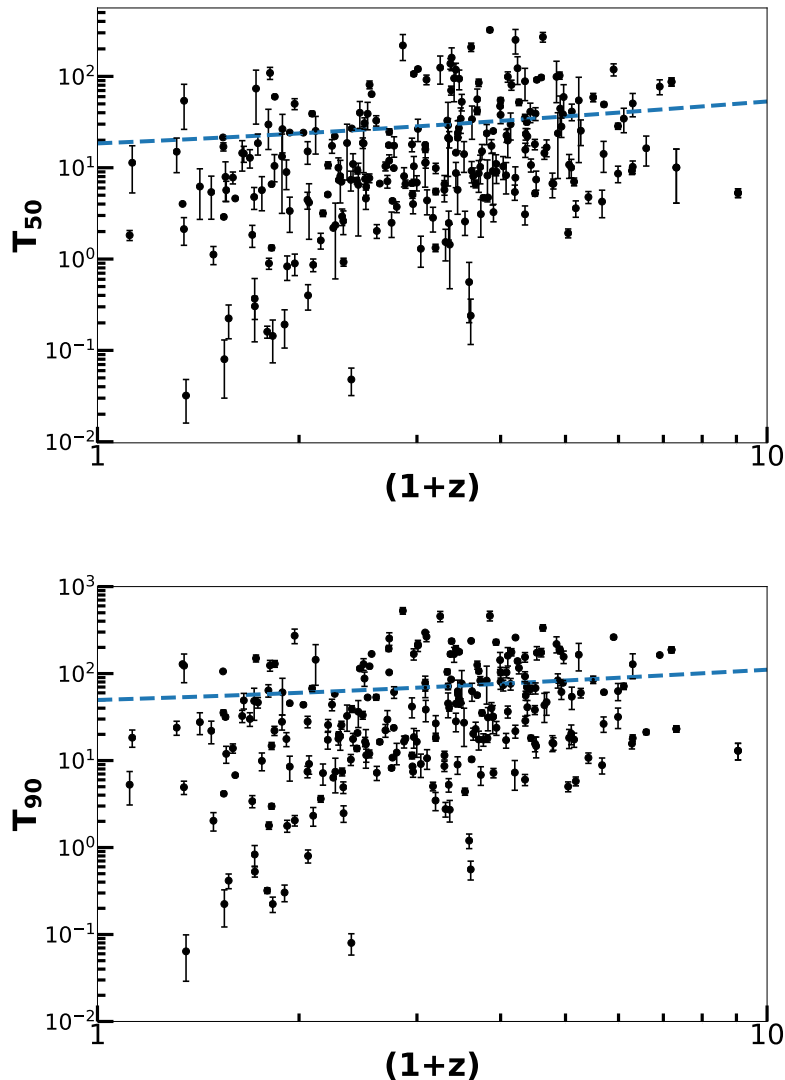


FIG. 9: Figure showing the relationship between the burst intervals, T_{90} and T_{50} in observer energy range (denoted by T_{90} , T_{50}), for long GRBs which had $T_{90,raw} > 2$ seconds. Through curve fitting, we obtain $T_{50} = 12.01(1+z)^{0.62}$ and $T_{90} = 35.86(1+z)^{0.47}$.

- **Analysis using geometric mean binned data for all GRBs**

Ref. [40] pointed out that any weighted mean would be affected by outliers and one should instead use more robust estimates such as geometric mean and median. For this purpose, we also redo our search for cosmological time dilation analysis by considering the geometric mean of T_{50}/T_{90} in each redshift bin. The contours for A and B after such a regression analysis can be found in Fig. 13 and Fig. 14 for T_{50} and T_{90} respectively. For T_{50} the intrinsic scatter we get from this fit is $< 60\%$. For T_{90} , the intrinsic scatter which get is $\ln(\sigma_{int}) = 1.84_{-1.33}^{+0.55}$. Although the best-fit value of the scatter is greater than 100%, it is consistent with 27% to within 68% c.l. Therefore, we get the tightest scatter using the geometric mean for both T_{50} and T_{90} . The power-law exponent (B) we get is consistent with a cosmological signature, for T_{50} and T_{90} to within 1σ . The burst intervals as a function of redshift $(1+z)$ are shown in Fig. 15 along with the best-fit.

The results of all our regression analyses using both the unbinned as well as binned data are summarized in Tables I and II, respectively. For the unbinned analyses, the intrinsic scatter is $> 100\%$, which implies that we cannot draw any definitive conclusion between durations and redshifts. Our main result is that only after using the geometric mean

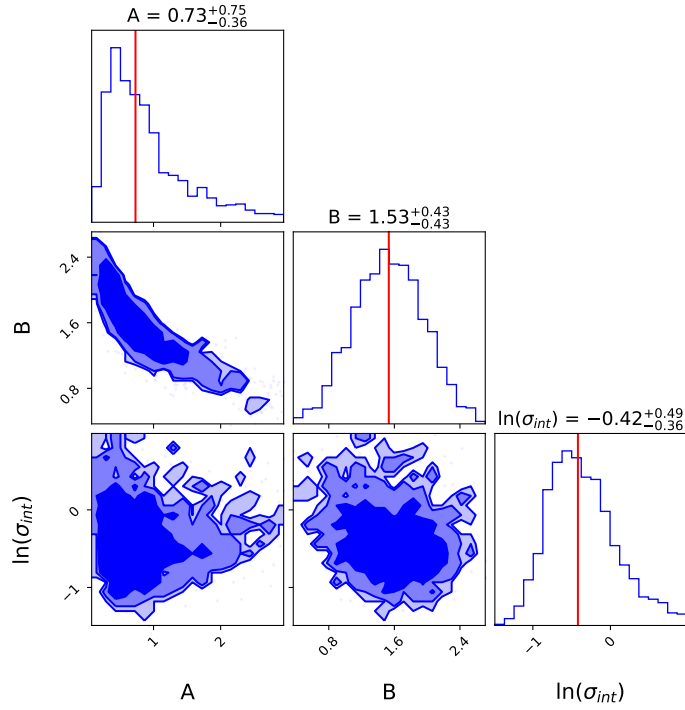


FIG. 10: Plot showing 68%, 90%, and 95% credible intervals for A and B for T_{50} in the rest frame energy range of 140-350 keV, using the binned redshift data (containing 6 groups equally spaced in z), for long GRBs. The intrinsic scatter is 65.7%. The value of B is consistent with a cosmological time dilation signature within 1σ .

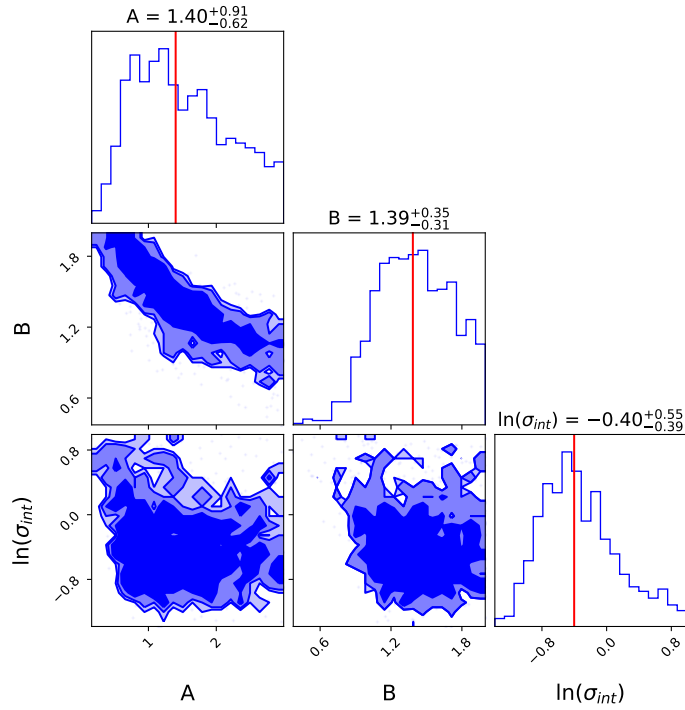


FIG. 11: Plot showing 68%, 90%, and 95% credible intervals of A and B for T_{90} with the binned redshift data (containing 6 groups equally spaced in z), for long GRBs. The intrinsic scatter is equal to 67.03%. The value of B is consistent with a cosmological time dilation signature within 1σ .

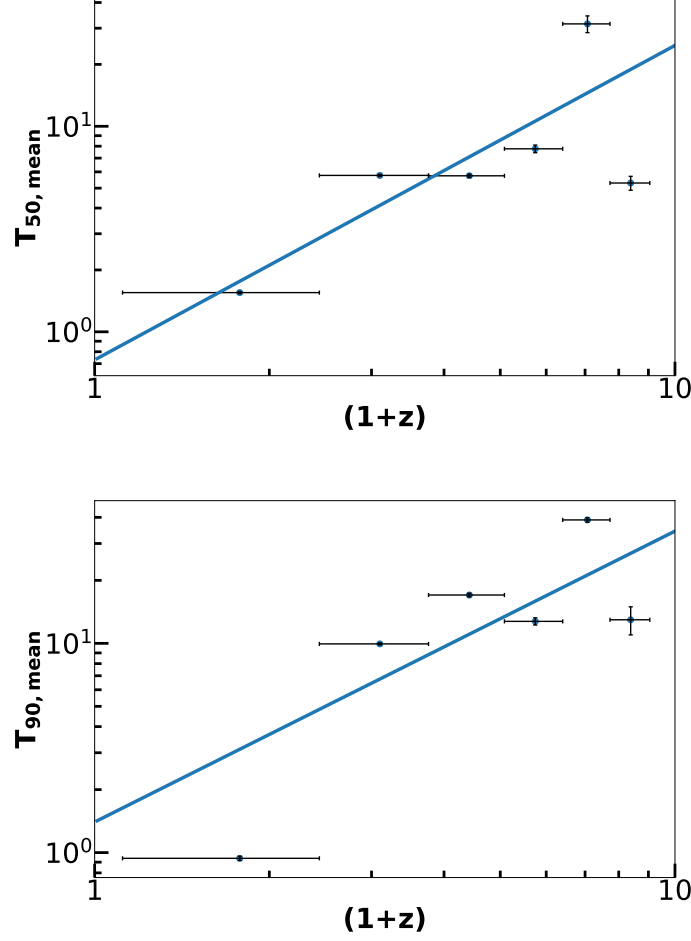


FIG. 12: Plots showing weighted means of burst intervals using only the long GRB sample, with the binned redshift data (containing 6 groups equally spaced in z), where the horizontal error bars denote the redshift range in each group. . The blue line is the best fit curve obtained through the estimation of parameters A and B (cf. Eq. 1). We obtain $T_{50} = 0.73(1+z)^{1.53}$ and $T_{90} = 1.40(1+z)^{1.39}$.

TABLE I: Table showing a summary of best fit values of A , B , and the logarithm scatter (σ_{int}) for different kinds of analysis for unbinned GRB datasets.

Dataset	$A_{T_{50}}$	$B_{T_{50}}$	$\ln \sigma_{int, T_{90}}$	$A_{T_{90}}$	$B_{T_{90}}$	$\ln \sigma_{int, T_{90}}$
Full Sample	$11.01^{+2.74}_{-2.53}$	$0.66^{+0.17}_{-0.17}$	$3.42^{+0.5}_{-0.6}$	$32.96^{+7.82}_{-6.66}$	$0.52^{+0.15}_{-0.16}$	$4.24^{+0.05}_{-0.05}$
Long GRBs	$12.01^{+3.14}_{-2.76}$	$0.62^{+0.18}_{-0.17}$	$3.44^{+0.06}_{-0.05}$	$35.86^{+7.30}_{-7.15}$	$0.47^{+0.15}_{-0.14}$	$4.25^{+0.06}_{-0.05}$

based binned data (full sample)¹ and weighed mean based binned data (long GRBs), we find evidence for cosmological time dilation for both these GRB durations. Among the binned analyses the data obtained using geometric mean show the smallest scatter. Therefore, we concur with Z13, that GRBs show evidence for cosmological time dilation only in a statistical sense, but not on a per-GRB basis.

¹ We have not done a geometric mean-based analysis on only long GRBs, but we would expect our conclusions to be the same as those with the full sample.

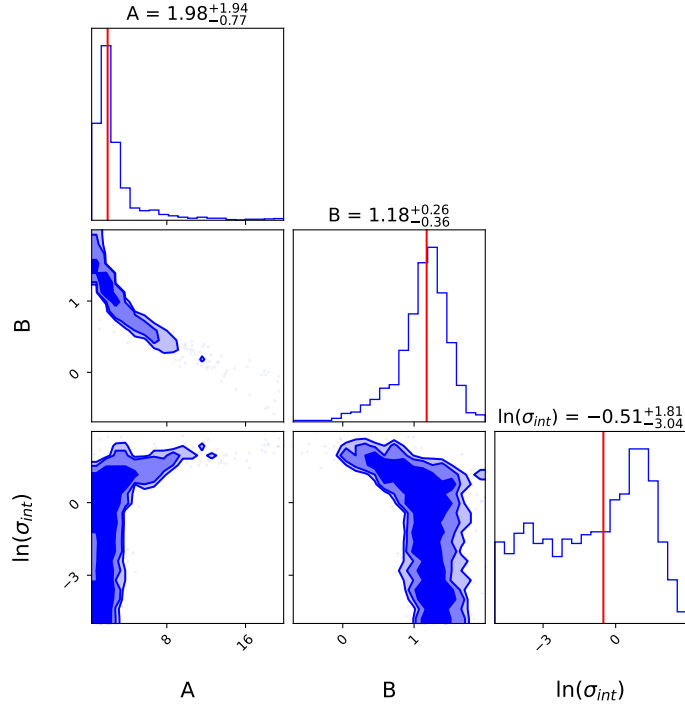


FIG. 13: Contours for 68%, 90%, and 95% credible intervals T_{50} in the rest frame energy range of 140-350 keV, using binned data where the geometric mean of T_{50} in each bin was used. The intrinsic scatter (σ_{int}) is very low, indicating that there is a deterministic relationship between binned durations and the redshifts. The value of B is consistent with the cosmological time dilation signature.

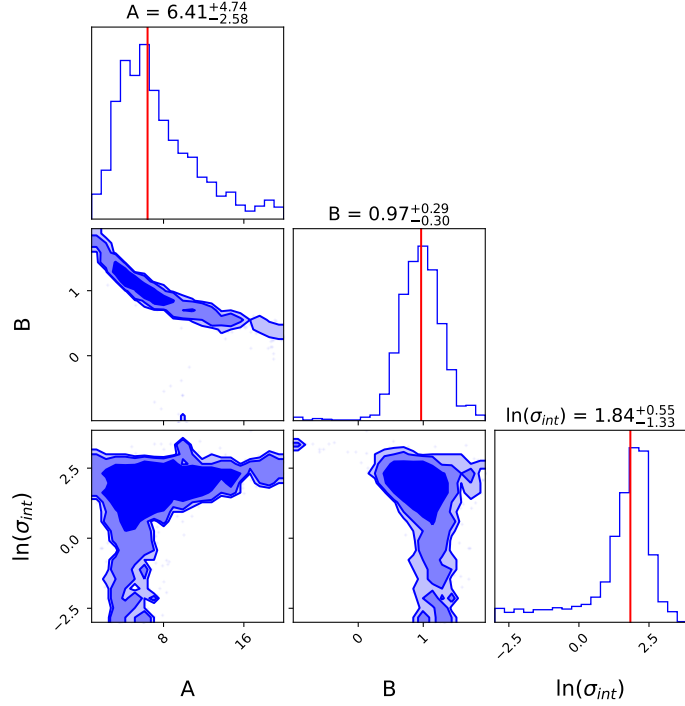


FIG. 14: Contours showing 68%, 90%, and 95% credible intervals for A and B for T_{90} in the rest frame energy range of 140-350 keV, using binned data where geometric mean of T_{90} in each bin was used. Although the median intrinsic scatter is greater than 100%, it is consistent within 1σ . However, the value of B is consistent with the cosmological time dilation signature to within 1σ .

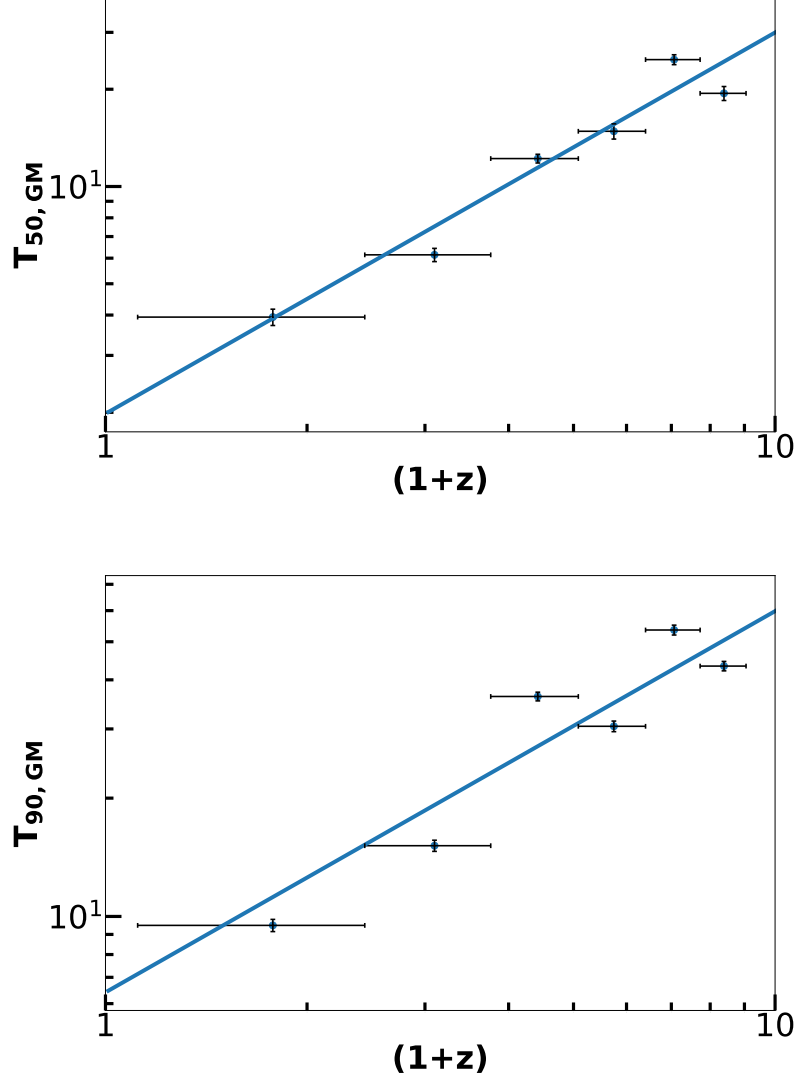


FIG. 15: Plots showing geometric means of burst intervals with the binned redshift data (containing 6 groups equally spaced in z), where the horizontal error bars denote the redshift range in each group. The blue line is the best fit curve obtained through the estimation of parameters A and B (cf. Eq. 1). We obtain $T_{50} = 1.98(1+z)^{1.18}$ and $T_{90} = 6.41(1+z)^{0.97}$.

TABLE II: Table showing a summary of best fit values of A , B , and the logarithm of intrinsic scatter (σ_{int}) for different kinds of analysis for binned GRB datasets. Note that the first two rows use the weighted mean in each redshift bin. The values of B are consistent with a cosmological time dilation signature for long GRBs and using geometric mean

Dataset	$A_{T_{50}}$	$B_{T_{50}}$	$\ln \sigma_{int, T_{50}}$	$A_{T_{90}}$	$B_{T_{90}}$	$\ln \sigma_{int, T_{90}}$
Full Sample	$0.40^{+0.62}_{-0.24}$	$1.79^{+0.55}_{-0.54}$	$-0.27^{+0.55}_{-0.41}$	$0.74^{+0.61}_{-0.38}$	$1.74^{+0.45}_{-0.36}$	$-0.40^{+0.49}_{-0.36}$
Long GRBs	$0.73^{+0.75}_{-0.36}$	$1.53^{+0.42}_{-0.44}$	$-0.42^{+0.49}_{-0.36}$	$1.40^{+0.91}_{-0.62}$	$1.39^{+0.35}_{-0.31}$	$-0.40^{+0.55}_{-0.39}$
Geometric mean binning	$1.98^{+1.94}_{-0.77}$	$1.18^{+0.26}_{-0.36}$	< -0.51	$6.41^{+4.74}_{-2.58}$	$0.97^{+0.29}_{-0.30}$	$1.84^{+0.55}_{-1.33}$

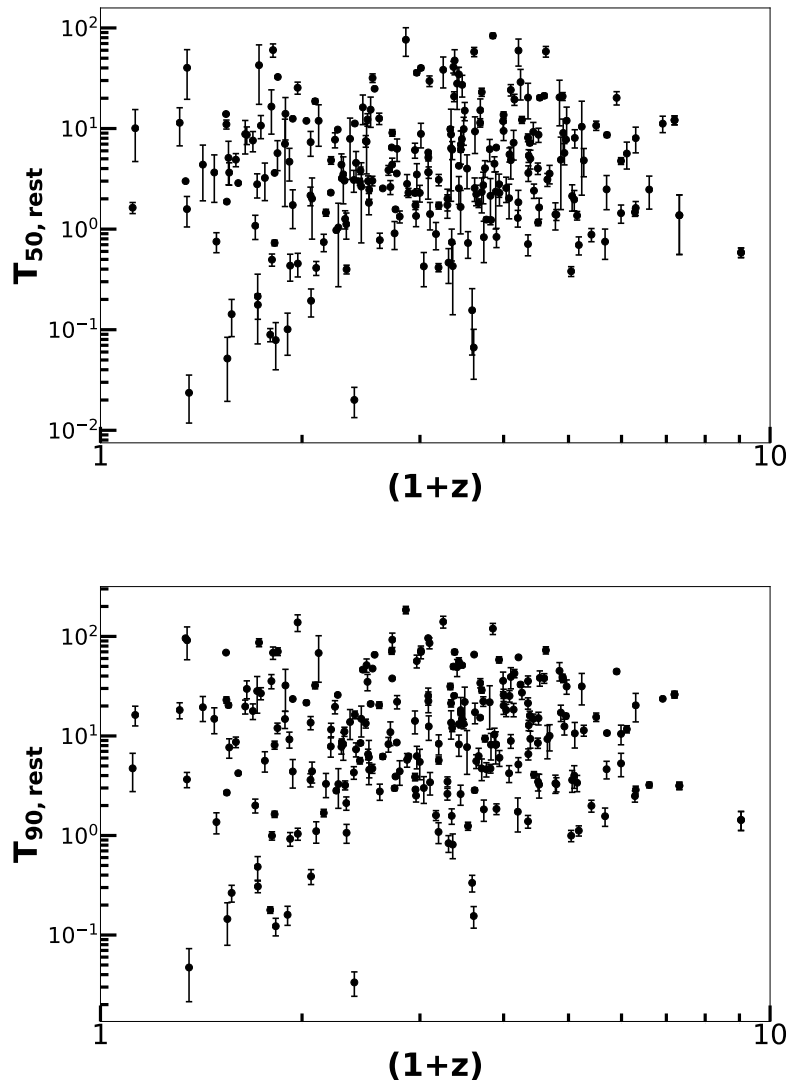


FIG. 16: Plots showing the correlations between $T_{50,rest}$ and $T_{90,rest}$ in the rest frame of GRBs with the redshifts. The rest frame durations are obtained by dividing the T_{50}/T_{90} tabulated in the last two columns of Table III by $(1+z)$.

A. Tests with rest frame durations

Similar to Z13, we carry out some additional tests to completely ascertain the redshift evolution of the intrinsic GRB duration, as found from some of the binned analyses. We calculate the rest frame $T_{90,rest}$ and from the T_{90} determined earlier using $T_{90,rest} = T_{90}/(1+z)$ (and same for T_{50}). These rest-frame durations are shown in Fig. 16. Similar to Z13, we find a large dynamic range in the durations with median values of 3.8 and 10 seconds for $T_{50,rest}$ and $T_{90,rest}$, respectively, while the standard deviations are 13 and 27 seconds for $T_{50,rest}$ and $T_{90,rest}$ respectively. We also checked for an evolution effect of the rest frame durations with redshifts using the same procedure as done for T_{50} and T_{90} earlier. The best-fit values for B are equal to $0.11^{+0.20}_{-0.19}$ and $-0.11^{+0.18}_{-0.17}$ for $T_{50,rest}$ and $T_{90,rest}$ respectively. Therefore, the values of B are significantly different from that expected from cosmological time dilation ($B = 1$). Furthermore, the logarithm of the intrinsic scatter is given by $\ln(\sigma_{int})$ is equal to $3.12^{+0.05}_{-0.05}$ and $2.17^{+0.06}_{-0.05}$ for $T_{50,rest}$ and $T_{90,rest}$ respectively, implying that the intrinsic scatter is greater than 100%. Therefore, This implies that there is no evolution of the rest frame durations, in accord with Z13's conclusions.

Finally, we check for any possible redshift evolution of rest-frame duration estimated directly from the raw durations (i.e. $T_{50,raw}/(1+z)$) as a function to redshift to independently confirm if we see a decreasing trend as found in some

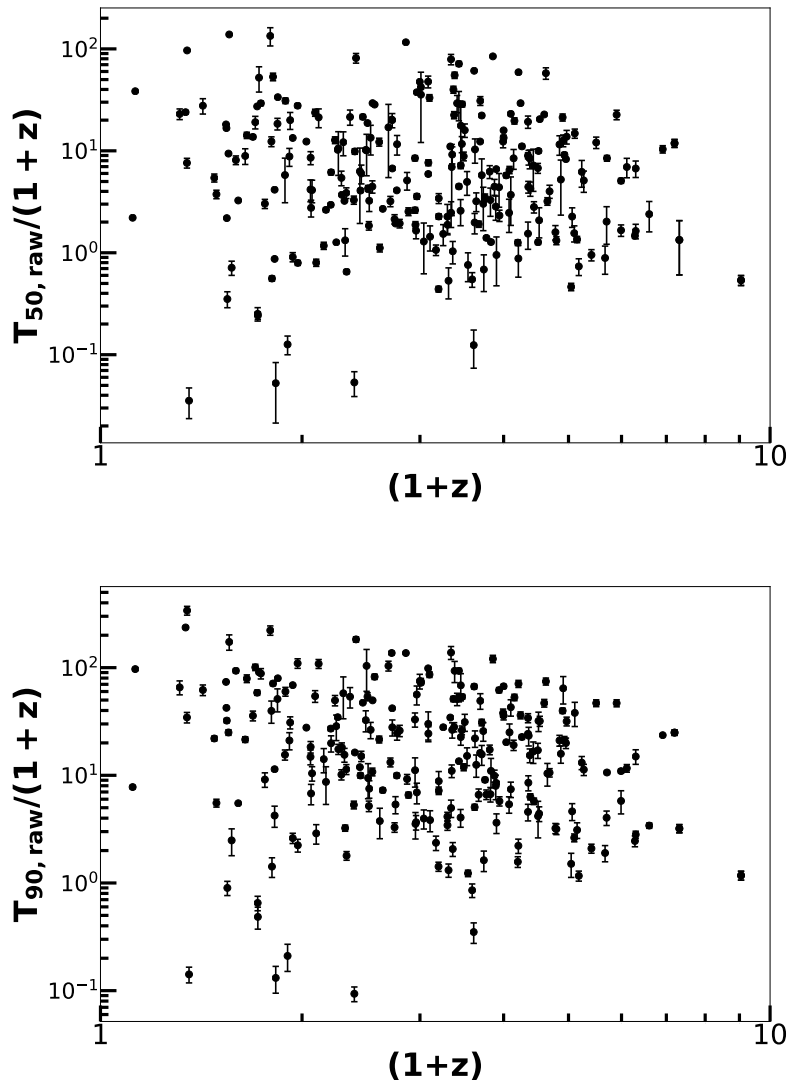


FIG. 17: Plots showing the correlations between the durations in the rest frame obtained using $T_{90,raw}/(1+z)$, (where “raw” indicates data measured between 15-350 keV in the observer frame), and the redshifts. All symbols carry the usual meaning.

previous works [35, 46]. These $T_{50,raw}/(1+z)$ and $T_{90,raw}/(1+z)$ plots can be found in Fig. 17. We find that B is equal to $-0.59^{+0.21}_{-0.21}$ and $-0.82^{+0.13}_{-0.10}$ for $T_{50,raw}/(1+z)$ and $T_{90,raw}/(1+z)$, respectively. Furthermore, the logarithm of the intrinsic scatter is given by $\ln(\sigma_{int})$ which is equal to $2.91^{+0.04}_{-0.05}$ and $3.55^{+0.05}_{-0.05}$. Therefore, we again concur with Z13, that there is no evidence that the measure of rest frame duration analyzed in [35, 46] shows any evolution with redshift.

III. CONCLUSIONS

Even though we know for more than two decades that almost all GRBs are located at cosmological distances, the cosmological time dilation signature for GRBs has not been unequivocally demonstrated. Therefore, we independently carry out a study similar to Z13 (and also [40]), using the latest updated GRB sample from the Swift satellite. We estimated T_{50} and T_{90} for all the GRBs in the Swift catalog, for the energy band of 140-350 keV in the rest frame. This corresponds to an energy band of $140/(1+z)$ and $350/(1+z)$ in the observer frame. These T_{50} and T_{90} intervals calculated for all the Swift GRBs are tabulated in Table III.

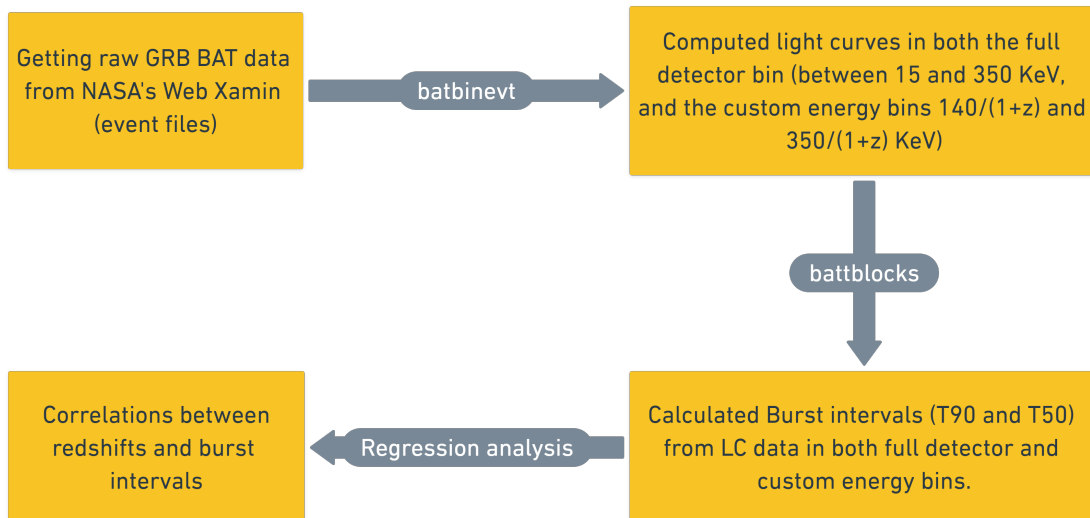


FIG. 18: A brief data processing pipeline for our analysis of the GRB samples obtained from the latest Swift catalog. The yellow boxes denote the type of products obtained and the black pointers represent the type of command used to generate those products.

We then carry out a regression analysis between the duration and redshifts using $T_{90}(T_{50}) = A(1+z)^B$ using both the unbinned and binned durations, where the binning was done using both a error weighted-mean as well as geometric-mean based average. We also analyzed the full sample as well as only the long GRB sample. For a cosmological time dilation signature, B should be equal to one. Our results from all these myriad analyses are summarized in Table I and Table II for the unbinned and the binned data, respectively. We conclude that the burst intervals obtained from the geometric mean-based and weighted mean-based (long GRBs) binned analyses are consistent with the cosmological time dilation phenomenon (within 1σ) for both T_{50} and T_{90} . (cf. Table II). The smallest intrinsic scatters are obtained using the geometric mean based binned data. The weighted mean analysis for the full sample is discrepant with respect to the cosmological time signature at 1.2σ and 2σ for T_{50} and T_{90} , respectively. The unbinned analyses show intrinsic scatters $> 100\%$ as well as values of B significantly different from 1, implying that no definitive conclusion between the durations and the redshifts can be inferred.

Finally, we should point out that although choosing a fixed energy frame interval may avoid the biases associated by recording different parts of the GRB intrinsic light curves, our results could still be affected by detector related selection biases. As Z13 pointed out for GRBs at higher redshifts and low SNRs, only the brightest GRBs would be detected and some of the observations could be underestimated. Secondly, the BAT effective area is energy dependent and drops sharply at energies less than 25 keV and greater than 100 keV [47]. Another possibility, pointed out in [40] is that the measured duration of a GRB could also be affected by the gradual loss of the final fast-rise exponential decay pulse tail due to the degraded signal-to-noise ratio [48]. A detailed modeling of these effects is beyond the scope of this work. However in a future work, we shall be using the deconvolved photon fluxes for estimating T_{90} , which could get rid of these instrumental effects [49].

All the codes which are utilized in this analysis, including the `batbinevt` and `battblocks` code generators have been made publicly available and can be found at [GRB Analysis Code \(Github\)](#).

ACKNOWLEDGEMENT

We are grateful to I-Non Chiu for useful correspondence about this work. We thank Amy Lien for help regarding Swift GRB database and `battblocks` command. We would also like to acknowledge Eleonora Troja, for assistance regarding GRB redshift data. We also appreciate the Swift Help team for their prompt response to all our queries. Finally, we are grateful to the anonymous referee for several constructive feedback on this manuscript.

Appendix A: Data retrieval and light curve analysis

We now describe the detailed step-by-step procedure for downloading the Swift light curve data and estimating T_{50}/T_{90} for every GRB. Fig. 18 demonstrates a brief workflow of this processing pipeline, starting from raw GRB event data to the calculation of the burst intervals. We have sampled 247 of the 400 GRBs which were eligible for the analysis (containing proper redshift data). The remaining 153 GRBs could not be processed, because most of the data products (101) for the remaining GRBs did not contain any TDRSS messages, and many (52) did not have data products with enough exposure to construct detailed Bayesian blocks, needed for the estimation of durations.

We use the Burst interval data recorded by the Burst Alert Telescope (BAT) aboard Swift. The BAT instrument has two basic modes of operation: 1) scan-survey mode and 2) burst mode. These two modes reflect the two major types of data that BAT produces: hard X-ray survey data and burst positions. Most of BAT's time is spent in waiting for a burst to occur in its FOV. Finding GRBs within BAT consists of two processes: 1) the detection of the onset of a burst by looking for increases in the event rate across the detector plan, and 2) the formation of an image of the sky using the events detected during the time interval at the beginning of the burst. [50]

Burst Trigger Algorithm:- The burst trigger algorithm looks for detector count rate excesses that are higher than those predicted from the background and constant sources. The fluctuations in the background and the heterogeneity of the GRB time profiles are the two fundamental barriers in GRB detection. During the 90-minutes the satellite stays in Low Earth Orbit, the detector background rates can change by more than a factor of two. GRBs can last anywhere from a few milliseconds to several minutes, with anywhere from one to several dozen peaks in the emission. As a result, the triggering system must be capable of extrapolating the background and comparing it to the recorded detector count rate over a wide range of timescales and energy bands [50].

NASA maintains an updated list of all the BAT observations at the Swift Archive [51]. We use **Web Xamin** [52], which acts as a source for downloading or saving the BAT GRB data for analysis, and **Web Hera** [53] (containing the HEASOFT tools from NASA) to analyze the BAT data. HEASOFT tools provided at <https://heasarc.gsfc.nasa.gov/docs/tools.html> work on a Linux machine but this analysis has explicitly made use of the Web Hera interface, owing to its simplicity and minimal computational resources at the user's end. The whole analysis can be classified into the following stages in chronological order:

- **Querying for and collecting the full GRB data products at the Swift archive through the Web Xamin interface**

For this access the Web Xamin at <https://heasarc.gsfc.nasa.gov/xamin/>.

We have to focus on the Query Pane for our queries.

After we have logged in, we can obtain a table of our interest through the **Table Explorer** option. Now there are multiple options to get the data. We can navigate through the folders in the **Table Explorer** to get the whole catalogue or search a GRB by its name (ex- GRB 050126) or its coordinates in the Target for search. To get the whole catalogue, we would go to **Popular Missions** → **Swift** → **Swiftbalog** to obtain the data for all the GRBs observed till date. Or if we search for a particular GRB, we can type the name and then click on 'search on all HEASARC tables' to run our query. For example, if we want to search and download the data for GRB 050319, then when we query for the GRB, we can find all the summary tables related to the GRB.

In this case too, out of all other tables, we just need the **Swiftbalog** table for getting the BAT GRB data. When we open the **Swiftbalog** table, we get a list of multiple data products. To figure out which event data has data products available, we need to look at the data products; they must contain a folder named as 'TDRSS'. This would most probably be one of the long exposure files (1000-2900 seconds). This is necessary because **batgrbproduct** will only work on those data products that contain this folder. Then, once we have found that particular data product, we can select it and click on 'Save to Hera'. This will save the data product to Web Hera, where we can further analyse the BAT GRB data.

- **GRB Analysis in Web HERA to calculate the observer frame energy binned and full detector range light curves**

To run any command, we can use either the Command Window Terminal or the Tool Parameter. For now, we will use Tool Parameter. Type '**batgrbproduct**' and click on Get.

We then run **batgrbproduct** keeping all the parameters to their default value. We just have to specify the input folder, where the raw data lies and another folder where the output files will be stored.

We then go to the results folder and save the file process.log to our local storage or view it elsewhere; we will then find the whole set of operations that **Hera** has performed using **batgrbproduct** command in the process.log file. We then find out the **batbinevt** command (used to prepare custom light curves in user-defined energy bins). A sample **batbinevt** command with its parameters looks like:


```

batbinevt infile='./00103780000-results/events/sw00103780000b_all.evt' outfile
↳='./00103780000-results/lc/sw00103780000b_bb_4ms.lc' outtype=LC timedel=0.004
↳timebinalg=u energybins='15-350' detmask='./00103780000-results/auxil/
↳sw00103780000b_qmap.fits' ecol=ENERGY weighted=YES outunits=RATE clobber=yes

```

Notice the parameters `energybins` and `timedel`. `energybins` are used to specify the energy range, and `timedel` is used to specify the Δt (the time resolution in seconds). The keyword `LC` denotes a light curve. These light curve files have an extension `.lc`. For short GRBs, we use 16 ms binned light curves, while for long GRBs, we use 64 ms binned light curves (following the same convention as in [3]). This, along with the output name, can be changed to produce the required light curves.

To calculate the light curves for obtaining the raw T_{50} and T_{90} (full detector energy range of 15-350 keV), we just have to copy and paste the command, without changing the energy ranges, copy the command, and run it in Hera. This will create the custom light curves that will be required for raw T_{90} calculation (in the folder light curves).

- **Calculation of burst intervals in rest frame and observer frame energy intervals**

For calculation of T_{90} and T_{50} in the rest frame energy interval of 140-350 keV, corresponding to a redshift-dependent observed energy range, we have to alter the energy bins $E_1 = 140/(1+z)$ and $E_2 = 350/(1+z)$. E_1 is the lower limit of the observed energy range, and E_2 is the upper limit. We make use of the newly created light curves to calculate estimated burst intervals (T_{90} and T_{50}) in the different energy ranges using the Bayesian block algorithm [54].

Now using the custom light curve file that we created, we will run the `battblocks` command. The input file would be the custom light curve file. We have to specify any desired name to the `durfile` as well as `output` file. Also, we have to make sure that we don't give an `optional filter`, which implies that the field should be completely empty (without any text). Click on run `battblocks`, and this should give the T_{90} and T_{50} for the GRB as the final result in the Hera command console.

TABLE III: Durations of 247 Swift GRBs with known redshifts evaluated in different energy bins. T_{50} and T_{90} are evaluated in rest frame energy interval of 140-350 keV and $T_{50,raw}$, $T_{90,raw}$ are evaluated in full detector range of BAT, 15-350 keV. We note that we have omitted GRB 130610A and GRB 160410A, as they yielded completely different T_{90} s in the observer frame compared to the SWIFT table. Also we omitted the GRBs 150403A, 180205A and 190106A because their data products could not be found on NASA's Swift database anymore.

GRB Name	Obs ID	z	$T_{90,raw}$ (s)	$T_{50,raw}$ (s)	E_1^* (keV)	E_2^* (keV)	T_{90} (s)	T_{50} (s)
050126	103780	1.29	23.248 ± 2.53	12.432 ± 2.036	61.14	152.84	17.808 ± 2.771	10 ± 2.815
050315	111063	1.949	97.248 ± 14.637	24.976 ± 1.471	47.47	118.68	41.744 ± 10.809	18 ± 3.065
050318	111529	1.44	29.056 ± 0.472	15.344 ± 10.616	57.38	143.44	13.776 ± 1.018	7.216 ± 0.588
050319	111622	3.24	153.072 ± 11.31	124.304 ± 4.228	33.02	82.55	139.184 ± 6.598	122.784 ± 41.306
050401	113120	2.9	33.12 ± 1.037	25.792 ± 0.588	35.90	89.74	32.032 ± 0.77	25.232 ± 0.497
050505	117504	4.27	59.53 ± 7.108	26.992 ± 6.363	26.57	66.41	59.928 ± 7.541	25.408 ± 7.939
050525A	130088	0.606	8.832 ± 0.081	5.232 ± 0.0226	87.17	217.93	6.784 ± 0.136	4.608 ± 0.086
050730	148225	3.968	157.584 ± 14.77	68.352 ± 10.465	28.18	70.45	155.904 ± 25.613	59.472 ± 21.642
050802	148646	1.52	18.928 ± 3.494	8.16 ± 1.765	55.56	138.89	11.536 ± 1.981	6.208 ± 1.216
050803	148833	0.422	88.176 ± 9.982	39.392 ± 6.757	98.45	246.13	27.632 ± 7.789	6.224 ± 3.507
050814	150314	5.3	94.208 ± 14.575	42.256 ± 7.78	22.22	55.56	127.936 ± 40.738	50.544 ± 14.466
050820A	151207	2.6147	241.36 ± 12.277	220.56 ± 3.117	38.73	96.83	237.52 ± 4.766	229.298 ± 22.092
050904	153514	6.2	179.5 ± 10.3	85.4 ± 7.6	19.44	48.61	187.744 ± 14.269	87.216 ± 8.845
050908	154112	3.35	19.9 ± 3.5	6.7 ± 2	32.18	80.46	6.032 ± 0.883	3.088 ± 0.727
050915A	155242	2.5273	53.424 ± 10.044	17.488 ± 4.585	39.69	99.23	27.232 ± 12.728	14.096 ± 5.21
050922C	156467	2.198	4.544 ± 0.442	1.408 ± 0.09	43.78	109.44	3.472 ± 0.821	1.328 ± 0.124
051001	157870	2.4296	178.656 ± 13.787	99.248 ± 31.747	40.82	102.05	191.52 ± 17.696	118.464 ± 20.638
051006	158593	1.059	30.56 ± 4.81	8.582 ± 2.079	67.99	169.99	7.456 ± 1.129	4.448 ± 0.936
051109A	163136	2.346	36.8 ± 4.959	23.2 ± 15.454	41.84	104.60	5.264 ± 0.931	2.48 ± 0.867
051221A	173780	0.547	1.392 ± 0.21	0.544 ± 0.097	90.50	226.24	0.224 ± 0.102	0.08 ± 0.05
060115	177408	3.53	144.496 ± 15.553	92.592 ± 2.848	30.91	77.26	173.568 ± 30.4185	91.792 ± 4.46
060124	178750	2.297	13.632 ± 1.312	7.456 ± 2.368	42.46	106.16	8.64 ± 1.169	5.728 ± 1.504
060206	180455	4.046	7.6 ± 1.919	2.336 ± 0.195	27.74	69.36	5.024 ± 0.653	1.92 ± 0.215

060210	180977	3.91	315.596 ± 90.034	62 ± 8.17	28.51	71.28	181.432 ± 13.453	44.4 ± 16.55
060223A	192059	4.41	11.312 ± 1.087	5.152 ± 0.653	25.88	64.70	10.752 ± 1.472	4.768 ± 0.715
060418	205851	1.49	80.977 ± 17.933	25.408 ± 0.736	56.22	140.56	33.296 ± 3.425	18.704 ± 2.479
060502A	208169	1.51	23.712 ± 8.501	10.752 ± 0.723	55.78	139.44	16.464 ± 2.016	7.536 ± 0.949
060510B	209352	4.9	275.984 ± 20.717	133.28 ± 14.292	23.73	59.32	262.096 ± 12.277	119.104 ± 18.044
060522	211117	5.11	71.12 ± 5.774	42.4 ± 9.166	22.91	57.28	71.44 ± 5.921	34.464 ± 10.305
060526	211957	3.21	298.08 ± 22.499	248.368 ± 8.458	33.25	83.14	259.392 ± 5.641	251.125 ± 75.339
060605	213630	3.78	15.392 ± 1.664	7.6 ± 1.233	29.29	73.22	15.984 ± 3.32	6.704 ± 2.02
060607A	213823	3.082	102.32 ± 20.047	26.528 ± 2.173	34.30	85.74	102.928 ± 13.706	22.56 ± 3.622
060614	214805	0.127	109.264 ± 3.415	43.296 ± 0.79	124.22	310.56	18.32 ± 4.113	11.344 ± 6.051
060707	217704	3.43	73.728 ± 16.668	31.856 ± 14.128	31.60	79.01	65.728 ± 7.743	41.024 ± 9.893
060714	219101	2.71	114.912 ± 7.97	82.368 ± 3.457	37.74	94.34	107.008 ± 6.919	85.408 ± 7.941
060719	220020	1.532	66.928 ± 11.558	34.048 ± 11.018	55.29	138.23	53.152 ± 2.271	39.954 ± 12.996
060814	224552	0.84	146.464 ± 4.768	61.792 ± 0.701	76.09	190.22	129.648 ± 11.505	59.92 ± 1.527
060904B	228006	0.703	171.504 ± 11.59	32.512 ± 4.59	82.21	205.52	3.408 ± 0.543	1.84 ± 0.498
060906	228316	3.685	49.568 ± 4.431	18.768 ± 2.763	29.88	74.71	46.944 ± 13.83	16.672 ± 3.488
060908	228581	1.8836	18.928 ± 1.155	7.312 ± 0.643	48.55	121.38	17.968 ± 1.056	6.64 ± 0.688
060912A	229185	0.937	5.056 ± 0.552	1.76 ± 0.182	72.28	180.69	8.512 ± 2.713	3.36 ± 1.401
060926	231231	3.208	9.328 ± 1.416	3.696 ± 1.272	33.27	83.17	21.776 ± 3.695	7.865 ± 2.454
060927	231362	5.6	22.528 ± 1.277	15.792 ± 5.217	21.21	53.03	21.248 ± 1.395	16.32 ± 5.891
061007	232683	1.261	78.32 ± 2.836	23.136 ± 0.192	61.92	154.80	58.432 ± 0.9	22.08 ± 0.352
061021	234905	0.3463	46.448 ± 5.2	10.24 ± 1.125	103.99	259.97	4.928 ± 0.861	2.128 ± 0.714
061110B	238174	3.44	25.504 ± 1.778	12.48 ± 1.584	31.53	78.83	18.128 ± 1.344	10.704 ± 1.742
061121	239899	1.314	35.888 ± 25.267	7.472 ± 0.121	60.50	151.25	25.5 ± 2.7	7.024 ± 0.172
061217	251634	0.827	0.24 ± 0.067	0.096 ± 0.057	76.63	191.57	0.224 ± 0.045	0.144 ± 0.071
061222A	252588	2.088	75.328 ± 12.018	23.632 ± 1.586	45.34	113.34	69.168 ± 16.343	15.904 ± 1.215
061222B	252593	3.355	37.168 ± 5.947	19.296 ± 2.544	32.15	80.37	28.624 ± 3.671	15.744 ± 2.787
070103	254532	2.6208	18.32 ± 1.14	7.168 ± 5.625	38.67	96.66	10.32 ± 0.563	9.248 ± 2.432
070110	255445	2.352	88.608 ± 14.379	30.8 ± 5.853	41.77	104.42	40.464 ± 3.442	20.656 ± 4.205

070129	258408	2.3384	460.976 ± 63.417	263.744 ± 30.857	41.94	104.84	71.136 ± 5.937	29.136 ± 22.829
070306	263361	1.497	259.408 ± 108.945	25.232 ± 11.025	56.07	140.17	128.496 ± 19.726	18.52 ± 9.651
070318	271019	0.838	94 ± 22.675	33.856 ± 4.432	76.17	190.42	22.064 ± 2.67	10.464 ± 3.458
070506	278693	2.31	4.352 ± 0.614	1.76 ± 0.593	42.30	105.74	2.768 ± 0.531	1.536 ± 0.582
070508	278854	0.82	20.736 ± 0.731	7.568 ± 0.147	76.92	192.31	14.768 ± 1.376	6.592 ± 0.147
070521	279935	0.553	38.832 ± 2.31	14.592 ± 0.307	90.15	225.37	31.68 ± 1.674	7.936 ± 3.661
070529	280706	2.4996	109.28 ± 19.698	55.776 ± 8.415	40.00	100.01	76.832 ± 31.453	52.688 ± 10.854
070611	282003	2.04	12.064 ± 2.426	3.92 ± 2.031	46.05	115.13	9.12 ± 2.737	1.292 ± 0.479
070714B	284856	0.92	59.392 ± 7.645	38.384 ± 7.273	72.92	182.29	1.776 ± 0.279	0.832 ± 0.249
070721B	285654	3.626	344.48 ± 25.742	267.2 ± 34.467	30.26	75.66	335.856 ± 27.91	269.888 ± 32.864
070802	286809	2.45	13.984 ± 2.625	8.912 ± 2.558	40.58	101.45	8.992 ± 2.053	5.728 ± 2.636
070810A	287364	2.17	7.488 ± 1.145	3.376 ± 0.4	44.16	110.41	5.056 ± 0.577	2.832 ± 0.857
071021	294974	2.452	236.48 ± 66.921	60.976 ± 37.908	40.56	101.39	62.752 ± 21.261	23.945 ± 8.677
071031	295670	2.692	181.488 ± 30.035	114.208 ± 11.346	37.92	94.80	125.6 ± 13.378	56.174 ± 16.555
071117	296805	1.331	4.176 ± 0.386	1.52 ± 0.071	60.06	150.15	2.48 ± 0.534	0.928 ± 0.093
080207	302728	2.0858	304.064 ± 8.824	147.344 ± 19.523	45.37	113.42	296.496 ± 9.744	11.339 ± 5.212
080210	302888	2.641	45.568 ± 10.652	11.648 ± 2.433	38.45	96.13	20.352 ± 3.224	8.08 ± 1.863
080310	305288	2.43	320.56 ± 16.622	244.912 ± 13.281	40.82	102.04	28.208 ± 6.805	8.742 ± 2.677
080319B	306757	0.937	133.2 ± 3.638	25.904 ± 0.124	72.28	180.69	45.552 ± 0.385	24.256 ± 0.249
080319C	306778	1.95	32.88 ± 9.962	7.712 ± 0.492	47.46	118.64	11.424 ± 0.985	6.752 ± 0.374
080411	309010	1.03	56.288 ± 0.903	25.025 ± 0.715	68.97	172.41	43.84 ± 2.086	24.208 ± 0.232
080413A	309096	2.43	46.352 ± 0.465	15.344 ± 0.749	40.82	102.04	45.104 ± 1.117	14.624 ± 0.315
080413B	309111	1.1	6.064 ± 1.245	1.68 ± 0.136	66.67	166.67	2.32 ± 0.563	0.864 ± 0.137
080430	310613	0.76	16.08 ± 2.475	5.328 ± 0.551	79.55	198.86	9.92 ± 2.294	5.68 ± 2.302
080516	311762	3.2	6.608 ± 0.753	5.28 ± 0.329	33.33	83.33	7.28 ± 2.727	5.424 ± 1.028
080603B	313087	2.69	59.504 ± 2.252	45.505 ± 1.124	37.94	94.85	56.368 ± 2.226	42.112 ± 4.018
080605	313299	1.6398	19.184 ± 0.924	7.12 ± 0.113	53.03	132.59	16.4 ± 0.972	6.704 ± 0.147
080607	313417	3.036	81.888 ± 2.675	23.184 ± 1.222	34.69	86.72	73.488 ± 10.46	10.336 ± 2.915
080804	319016	2.2	28.256 ± 6.43	10.944 ± 1.222	43.75	109.38	26.72 ± 6.104	9.904 ± 1.28

080810	319584	3.35	105.664 ± 3.074	38.976 ± 2.557	32.18	80.46	92.88 ± 12.074	35.28 ± 3.155
080905B	323898	2.374	94.704 ± 9.295	75.648 ± 6.082	41.49	103.73	85.6 ± 3.644	70.272 ± 7.92
080916A	324895	0.689	60.368 ± 6.296	23.136 ± 1.002	82.89	207.22	30.064 ± 5.38	12.832 ± 2.922
080928	326115	1.692	251.152 ± 61.419	47.888 ± 67.67	52.01	130.01	22.256 ± 3.759	10.384 ± 1.159
081008	331093	1.967	166.912 ± 33.379	111.296 ± 1.934	47.19	117.96	167.728 ± 24.736	106.416 ± 5.69
081029	332931	3.8479	102.176 ± 11.817	55.968 ± 12.126	28.88	72.20	218.656 ± 45.863	99.024 ± 47.465
081222	337914	2.77	24.992 ± 2.563	5.28 ± 0.2	37.14	92.84	17.44 ± 2.853	4.688 ± 0.264
090102	338895	1.547	27.44 ± 2.272	11.36 ± 1.569	54.97	137.42	11.968 ± 1.247	7.696 ± 0.848
090113	339852	1.7493	9.04 ± 0.915	5.872 ± 0.622	50.92	127.31	8.208 ± 0.452	2.446 ± 0.754
090205	342121	4.67	10.768 ± 1.848	5.04 ± 1.553	24.69	61.73	8.848 ± 1.848	4.256 ± 1.421
090418A	349510	1.608	56.192 ± 4.1	31.84 ± 2.843	53.68	134.20	53.328 ± 3.995	32.816 ± 4.264
090423	350184	8.05	10.624 ± 1.008	4.864 ± 0.544	15.47	38.67	12.96 ± 2.808	5.296 ± 0.581
090424	350311	0.544	49.744 ± 2.32	3.376 ± 0.057	90.67	226.68	4.16 ± 0.192	2.896 ± 0.115
090426	350479	2.609	1.264 ± 0.273	0.448 ± 0.182	38.79	96.98	0.56 ± 0.137	0.24 ± 0.124
090510	351588	0.903	0.4 ± 0.113	0.24 ± 0.05	73.57	183.92	0.304 ± 0.066	0.192 ± 0.086
090516A	352190	4.109	194.192 ± 49.188	75.648 ± 7.839	27.40	68.51	54.234 ± 13.563	41.13 ± 8.492
090519	352648	3.87	77.184 ± 14.151	25.456 ± 14.063	28.75	71.87	83.632 ± 15.633	23.808 ± 16.195
090529	353540	2.625	79.808 ± 13.905	37.408 ± 10.011	38.62	96.55	62.688 ± 14.664	33.904 ± 13.447
090530	353567	1.266	39.648 ± 4.278	23.952 ± 10.948	61.78	154.46	7.44 ± 3.193	2.352 ± 1.746
090618	355083	0.54	113.536 ± 0.585	27.952 ± 0.157	90.91	227.27	105.904 ± 1.841	21.456 ± 0.555
090715B	357512	3	268.256 ± 11.4	63.472 ± 1.191	35.00	87.50	80.528 ± 14.67	54.56 ± 4.011
090726	358422	2.71	58.064 ± 12.174	21.392 ± 9.522	37.74	94.34	17.488 ± 4.293	8.672 ± 3.298
090809	359530	2.737	6.08 ± 1.312	2.56 ± 1.005	37.46	93.66	6.832 ± 1.651	3.104 ± 1.369
090812	359711	2.452	78.144 ± 12.498	24.864 ± 1.296	40.56	101.39	58.736 ± 3.411	21.312 ± 1.234
090926B	370791	1.24	111.184 ± 12.297	28.528 ± 2.178	62.50	156.25	44 ± 6.677	17.344 ± 2.964
091018	373172	0.971	4.416 ± 0.602	1.568 ± 0.086	71.03	177.57	2.048 ± 0.283	0.896 ± 0.237
091020	373458	1.71	35.84 ± 3.3943	8.672 ± 1.006	51.66	129.15	29.584 ± 7.922	7.104 ± 1.129
091024	373674	1.092	113.696 ± 14.176	49.584 ± 3.924	66.92	167.30	67.36 ± 5.198	39.072 ± 2.257
091029	374210	2.752	34.048 ± 1.688	13.072 ± 1.069	37.31	93.28	35.296 ± 2.65	15.12 ± 2.852

091109A	375246	3.076	21.92 ± 3.808	10.048 ± 3.603	34.35	85.87	17.184 ± 3.321	8.272 ± 3.113
091127	377179	0.49	8.24 ± 0.69	5.584 ± 0.534	93.96	234.90	2.032 ± 0.486	1.12 ± 0.252
091208B	378559	1.063	13.984 ± 3	5.687 ± 1.071	67.86	169.66	0.8 ± 0.137	0.4 ± 0.124
100219A	412982	4.7	23.008 ± 3.529	11.52 ± 4.613	24.56	61.40	26.4 ± 5.314	14.16 ± 5.272
100413A	419404	3.9	194.976 ± 10.818	104.256 ± 8.3	28.57	71.43	190.368 ± 14.054	102.304 ± 9.234
100424A	420367	2.465	90.864 ± 8.578	40.48 ± 7.29	40.40	101.01	51.184 ± 6.691	27.216 ± 5.762
100615A	424733	1.398	39.088 ± 0.85	23.664 ± 1.463	58.38	145.95	39.168 ± 3.493	26.896 ± 1.133
100621A	425151	0.542	65.28 ± 1.8	25.76 ± 0.774	90.79	226.98	35.488 ± 2.588	16.976 ± 1.746
100728A	430151	1.567	211.312 ± 11.744	72.976 ± 1.227	54.54	136.35	168.112 ± 2.547	63.872 ± 1.188
100728B	430172	2.106	11.92 ± 2.637	4.464 ± 1.234	45.07	112.69	10.624 ± 2.709	4.384 ± 1.336
100816A	431764	0.8035	2.56 ± 0.531	1.008 ± 0.057	77.63	194.07	1.792 ± 0.172	0.896 ± 0.124
100901A	433065	1.408	440.672 ± 24.921	195.76 ± 21.302	58.14	145.35	17.664 ± 2.836	10.976 ± 3.251
100902A	433160	4.5	257.584 ± 18.765	66.432 ± 8.541	25.45	63.64	85.136 ± 8.32	58.896 ± 6.226
100906A	433509	1.727	114.304 ± 1.643	54.576 ± 8.698	51.34	128.35	103.184 ± 2.231	11.936 ± 1.898
101219A	440606	0.718	0.832 ± 0.192	0.416 ± 0.035	81.49	203.73	0.528 ± 0.071	0.304 ± 0.086
110128A	443861	2.339	16.592 ± 3.048	8.24 ± 2.33	41.93	104.82	45.408 ± 14.395	21.248 ± 13.229
110205A	444643	2.1	267.504 ± 16.17	102.72 ± 7.5	45.16	112.90	265.856 ± 33.4	92.128 ± 11.164
110422A	451901	1.77	27.552 ± 1.395	11.344 ± 0.262	50.54	126.35	23.792 ± 0.906	9.904 ± 0.24
110503A	452685	1.613	9.824 ± 3.091	2.912 ± 0.252	53.58	133.95	7.232 ± 1.339	2.032 ± 0.349
110715A	457330	0.82	7.696 ± 1.712	1.584 ± 0.045	76.92	192.31	2.976 ± 0.215	1.328 ± 0.086
110731A	458448	2.83	42.096 ± 12.84	4.88 ± 0.186	36.55	91.38	31.36 ± 9.328	4.72 ± 0.17
110801A	458521	1.858	390.512 ± 9.271	331.728 ± 7.321	48.99	122.46	527.44 ± 45.396	218.144 ± 69.01
110818A	500914	3.36	101.664 ± 20.021	37.792 ± 6.206	32.11	80.28	55.904 ± 6.68	23.456 ± 3.397
111008A	505054	4.9898	65.52 ± 2.73	30.432 ± 1.666	23.37	58.43	62.864 ± 14.042	28.528 ± 2.202
111107A	507185	2.893	31.072 ± 7.974	11.056 ± 2.946	35.96	89.90	31.584 ± 11.236	9.184 ± 5.284
111123A	508319	3.1516	219.776 ± 15.045	81.776 ± 5.775	33.72	84.30	176.416 ± 16.873	80.688 ± 10.225
111228A	510649	0.714	100.352 ± 5.475	46.768 ± 0.78	81.68	204.20	48.4 ± 19.393	4.779 ± 1.291
120118B	512003	2.943	22.672 ± 2.233	9.152 ± 1.164	35.51	88.76	23.808 ± 4.329	9.04 ± 2.33
120119A	512035	1.728	76.144 ± 12.945	18.32 ± 0.723	51.32	128.30	252.816 ± 41.751	24.752 ± 1.874

120326A	518626	1.798	72.736 ± 8.768	5.424 ± 0.522	50.04	125.09	12.352 ± 3.417	3.728 ± 0.508
120327A	518731	2.813	65.952 ± 6.777	23.824 ± 3.444	36.72	91.79	83.136 ± 38.614	23.776 ± 5.911
120404A	519380	2.876	38.386 ± 4.908	17.248 ± 3.077	36.12	90.30	40.016 ± 6.344	17.312 ± 2.991
120712A	526351	4.15	16 ± 2.651	6.96 ± 0.492	27.18	67.96	17.424 ± 3.239	7.024 ± 0.69
120729A	529095	0.8	71.44 ± 16.659	22.224 ± 2.455	77.78	194.44	64 ± 10.44	29.728 ± 13.899
120802A	529486	3.796	15.2 ± 1.712	6.32 ± 0.568	29.19	72.98	15.696 ± 2.553	6.672 ± 0.829
120805A	530031	3.1	30.448 ± 4.98	15.168 ± 7.564	34.15	85.37	36.544 ± 5.751	19.856 ± 6.959
120811C	530689	2.671	24.224 ± 3.175	7.008 ± 0.489	38.14	95.34	23.04 ± 4.555	6.672 ± 0.659
120815A	531003	2.358	6.944 ± 1.022	3.472 ± 0.861	41.69	104.23	2.72 ± 0.758	1.44 ± 0.967
120909A	533060	3.93	105.504 ± 7.571	45.088 ± 2.249	28.40	70.99	61.456 ± 61.113	28.176 ± 6.739
120922A	534394	3.1	175.808 ± 30.454	94.608 ± 4.037	34.15	85.37	160.464 ± 38.491	99.152 ± 12.865
121024A	536580	2.298	11.344 ± 1.18	6.208 ± 1.266	42.45	106.12	11.472 ± 1.319	6.608 ± 1.611
121027A	536831	1.773	68.432 ± 9.656	32.192 ± 7.014	50.49	126.22	61.184 ± 9.355	17.454 ± 4.37
121128A	539866	2.2	23.056 ± 1.843	7.264 ± 0.436	43.75	109.38	18.192 ± 1.497	5.488 ± 0.43
121201A	540178	3.385	27.712 ± 1.812	18.672 ± 2.977	31.93	79.82	41.024 ± 7.971	22.032 ± 4.686
130131B	547420	2.539	4.352 ± 0.3	2.688 ± 0.846	39.56	98.90	4.4 ± 0.409	2.576 ± 0.763
130427A	554620	0.34	316.272 ± 7.63	32.064 ± 1.296	104.48	261.19	128.336 ± 4.859	4.016 ± 0.079
130514A	555821	3.6	215.488 ± 17.628	104.56 ± 2.813	30.43	76.09	174.784 ± 19.402	97.344 ± 5.01
130603B	557310	0.356	0.192 ± 0.032	0.048 ± 0.016	103.24	258.11	0.064 ± 0.035	0.032 ± 0.016
130604A	557354	1.06	37.792 ± 4.627	17.632 ± 2.579	67.96	169.90	28.016 ± 4.249	15.088 ± 4.185
130606A	557589	5.913	163.088 ± 2.983	71.696 ± 5.921	20.25	50.63	163.344 ± 2.805	76.936 ± 14.425
130701A	559482	1.155	30.498 ± 7.721	2.528 ± 0.204	64.97	162.41	3.632 ± 0.315	1.6 ± 0.315
130831A	568849	0.4791	32.512 ± 1.689	8.032 ± 0.726	94.65	236.63	21.968 ± 6.399	5.408 ± 2.68
130925A	571830	0.347	456.752 ± 42.832	130.096 ± 2.671	103.93	259.84	123.136 ± 44.636	54.112 ± 27.817
131004A	573190	0.717	1.12 ± 0.172	0.432 ± 0.065	81.54	203.84	0.832 ± 0.222	0.368 ± 0.244
131030A	576238	1.293	41.808 ± 4.054	8.496 ± 0.227	61.06	152.64	19.696 ± 1.704	7.328 ± 0.222
131117A	577968	4.18	6.032 ± 0.644	3.808 ± 0.713	27.03	67.57	5.792 ± 0.679	3.6 ± 0.734
131227A	582184	5.3	17.744 ± 1.323	10.304 ± 1.681	22.22	55.56	18.096 ± 1.625	10.224 ± 1.625
140114A	583861	3	143.376 ± 12.658	53.664 ± 3.288	35.00	87.50	103.328 ± 14.59	37.888 ± 7.521

140206A	585834	2.73	96.096 ± 18.87	11.264 ± 19.12	37.53	93.83	83.072 ± 9.18	10.179 ± 3.544
140213A	586569	1.2076	59.92 ± 2.691	6.528 ± 0.272	63.42	158.54	17.312 ± 3.8	5.088 ± 0.227
140304A	590206	5.283	15.424 ± 1.793	9.232 ± 0.502	22.28	55.71	15.632 ± 2.044	9.264 ± 0.851
140419A	596426	3.956	98.816 ± 11.03	41.072 ± 1.356	28.25	70.62	78.624 ± 4.454	38.464 ± 1.402
140423A	596901	3.26	96.656 ± 4.8	47.136 ± 2.198	32.86	82.16	115.936 ± 16.846	52 ± 4.125
140506A	598284	0.889	113.232 ± 10.643	58.576 ± 3.623	74.11	185.28	60.784 ± 57.44	26.564 ± 11.931
140512A	598819	0.725	156.4 ± 4.609	90.08 ± 25.051	81.16	202.90	149.616 ± 13.693	73.52 ± 43.51
140515A	599037	6.32	23.456 ± 2.048	9.776 ± 5.341	19.13	47.81	23.136 ± 1.958	10.048 ± 5.955
140518A	599287	4.707	60.624 ± 2.409	48.24 ± 3.093	24.53	61.33	60.992 ± 2.595	49.312 ± 2.671
140614A	601646	4.233	68.64 ± 9.568	32.544 ± 9.56	26.75	66.88	164.752 ± 57.526	54.592 ± 43.213
140703A	603243	3.14	79.008 ± 8.665	34.96 ± 7.704	33.82	84.54	76.144 ± 11.648	29.904 ± 9.801
140907A	611933	1.21	43.888 ± 7.536	13.616 ± 0.784	63.35	158.37	25.648 ± 3.993	10.672 ± 0.917
141004A	614390	0.57	3.904 ± 1.091	1.12 ± 0.178	89.17	222.93	0.416 ± 0.08	0.224 ± 0.09
141026A	616502	3.35	148.16 ± 14.323	83.856 ± 11.565	32.18	80.46	154.704 ± 19.59	88.384 ± 34.148
141109A	618024	2.993	151.312 ± 13.295	49.168 ± 6.437	35.06	87.65	142.96 ± 31.975	47.28 ± 8.818
141220A	621915	1.3195	7.504 ± 0.489	3.072 ± 0.92	60.36	150.89	7.424 ± 0.77	2.928 ± 0.602
141221A	622006	1.452	36.928 ± 4.064	14.688 ± 3.075	57.10	142.74	36.432 ± 12.491	6.496 ± 4.708
141225A	622476	0.915	40.336 ± 7.33	16.848 ± 3.373	73.11	182.77	17.68 ± 3.238	8.96 ± 3.206
150206A	630019	2.087	92.72 ± 27.123	18.288 ± 0.656	45.35	113.38	78.128 ± 15.265	17.856 ± 0.444
150301B	633180	1.5169	13.04 ± 1.465	4.64 ± 0.443	55.62	139.06	15.424 ± 7.267	4.592 ± 1.098
150314A	634795	1.758	14.79 ± 2.681	5.344 ± 0.151	50.76	126.90	10.8 ± 0.349	4.336 ± 0.187
150323A	635887	0.593	149.12 ± 6.815	12.928 ± 1.264	87.88	219.71	13.84 ± 1.687	7.808 ± 1.165
150423A	638808	1.394	0.224 ± 0.035	0.128 ± 0.035	58.48	146.20	0.08 ± 0.022	0.048 ± 0.016
150727A	650530	0.313	86.128 ± 12.748	30.192 ± 3.624	106.63	266.57	23.904 ± 4.388	14.976 ± 6.15
150910A	655097	1.359	126.72 ± 27.241	50.64 ± 8.607	59.35	148.37	32.576 ± 10.868	18.64 ± 11.31
151021A	660671	2.33	114.56 ± 4.125	36.736 ± 1.245	42.04	105.11	104.672 ± 7.647	32.832 ± 1.545
151027A	661775	0.81	128.88 ± 5.924	96.352 ± 8.243	77.35	193.37	124.048 ± 17.66	109.04 ± 16.476
151027B	661869	4.063	23.424 ± 4.197	11.472 ± 2.494	27.65	69.13	18.256 ± 4.521	10.8 ± 3.158
151111A	663074	3.5	76.88 ± 12.341	30.448 ± 3.4	31.11	77.78	38.272 ± 4.518	18.064 ± 2.36

151112A	663179	4.1	13.424 ± 1.125	7.936 ± 1.431	27.45	68.63	20.4 ± 5.227	10.048 ± 2.301
151215A	667392	2.59	3.072 ± 0.443	1.968 ± 0.323	39.00	97.49	1.2 ± 0.229	0.56 ± 0.359
160121A	671231	1.96	10.848 ± 1.67	4.88 ± 0.823	47.30	118.24	7.44 ± 1.022	4 ± 0.871
160131A	672236	0.97	216.096 ± 21.979	54.64 ± 2.462	71.07	177.66	272.544 ± 51.957	50.096 ± 6.88
160203A	672525	3.52	19.92 ± 3.116	9.408 ± 3.083	30.97	77.43	14.672 ± 3.941	7.424 ± 2.75
160227A	676423	2.38	315.856 ± 70.295	186.464 ± 13.206	41.42	103.55	235.664 ± 13.489	160.352 ± 44.885
160327A	680655	4.99	34.64 ± 8.411	9.952 ± 1.282	23.37	58.43	31.712 ± 8.388	8.624 ± 1.773
160804A	707231	0.736	153.168 ± 16.881	50.784 ± 2.622	80.65	201.61	46.528 ± 6.453	18.56 ± 4.806
161014A	717500	2.823	25.52 ± 3.939	12.592 ± 3.887	36.62	91.55	17.984 ± 1.808	8.192 ± 3.969
161017A	718023	2.01	217.728 ± 6.527	126.64 ± 5.22	46.51	116.28	215.44 ± 13.341	120.416 ± 5.937
161117A	722604	1.549	126.672 ± 1.23	74.816 ± 0.523	54.92	137.31	121.104 ± 1.126	81.056 ± 7.988
161129A	724438	0.645	35.376 ± 2.128	14.656 ± 2.572	85.10	212.77	32.512 ± 5.204	14.48 ± 5.299
170113A	732526	1.968	20.592 ± 4.477	10.608 ± 0.649	47.17	117.92	18.608 ± 4.749	10.368 ± 2.902
170202A	736407	3.65	48.416 ± 11.521	14.864 ± 1.262	30.1	75.27	43.312 ± 15.926	14.48 ± 2.135
170405A	745797	3.51	144.48 ± 49.554	44.96 ± 2.055	31.04	77.61	68.352 ± 9.956	39.104 ± 6.281
170531B	755354	2.366	172.384 ± 9.642	134.208 ± 10.509	41.59	103.98	167.472 ± 9.085	138.032 ± 18.292
170604A	755867	1.329	26.48 ± 2.808	9.008 ± 1.087	60.11	150.28	4.928 ± 0.754	2.608 ± 0.758
170607A	756284	0.557	269.808 ± 43.921	215.632 ± 1.009	89.92	224.79	11.936 ± 2.638	5.68 ± 1.424
170705A	760064	2.01	224 ± 15.031	107.04 ± 70.704	46.51	116.28	210.048 ± 30.829	26.594 ± 7.351
170714A	762535	0.793	397.984 ± 39.658	240.352 ± 48.829	78.08	195.20	0.32 ± 0.024	0.16 ± 0.024
170903A	770528	0.886	29.264 ± 3.162	10.912 ± 5.073	74.23	185.58	27.904 ± 5.51	13.264 ± 10.102
171020A	780845	1.87	26.496 ± 2.718	14.704 ± 2.894	48.78	121.95	16.512 ± 2.588	8.08 ± 1.924
171222A	799669	2.409	174.112 ± 22.922	99.808 ± 19.292	41.06	102.67	167.232 ± 32.646	95.344 ± 42.602
180115A	805318	2.487	41.504 ± 3.066	30.832 ± 3.026	47.35	100.37	46.064 ± 5.001	34.432 ± 10.67
180314A	814129	1.445	24.368 ± 1.367	9.968 ± 0.4305	57.26	143.15	20.768 ± 0.958	9.328 ± 0.801
180325A	817564	2.25	90.8 ± 3.385	4.976 ± 1.159	43.07	107.69	455.968 ± 62.01	124.672 ± 42.425
180329B	819490	1.998	224.848 ± 35.111	142.768 ± 3.528	46.70	116.74	16.448 ± 5.562	6.864 ± 1.3
180510B	831816	1.305	133.152 ± 55.954	28 ± 7.388	60.74	151.84	19.056 ± 5.933	8.08 ± 3.97
180620B	843211	1.1175	229.968 ± 21.917	45.12 ± 9.44	66.12	165.29	144.208 ± 70.882	25.28 ± 11.174

180624A	844192	2.855	465.216 ± 36.332	325.552 ± 9.305	36.32	90.79	461.728 ± 59.093	322.544 ± 18.492
180720B	848890	0.654	130.864 ± 10.726	23.488 ± 1.649	84.64	211.61	49.12 ± 10.04	14.304 ± 2.846
180728A	850471	0.117	8.688 ± 0.321	2.464 ± 0.035	125.33	313.34	5.28 ± 2.197	1.824 ± 0.23
181010A	866434	1.39	12.704 ± 1.047	7.872 ± 0.723	58.57	146.44	10.256 ± 1.486	7.36 ± 1.809
181020A	867987	2.938	243.568 ± 13.439	17.296 ± 6.28	35.55	88.88	229.328 ± 16.505	11.008 ± 2.856
181110A	871316	1.505	134.768 ± 11.635	46.912 ± 1.436	55.89	139.72	87.616 ± 16.402	30.8 ± 4.379
190114A	930285	3.3765	70.416 ± 5.15	30.992 ± 1.143	31.99	79.97	70.08 ± 7.642	31.488 ± 1.681
190324A	927839	1.1715	299.984 ± 81.712	32.144 ± 27.954	64.47	161.18	7.168 ± 1.957	3.168 ± 0.25
190719C	915381	2.469	186.208 ± 9.309	99.456 ± 6.052	40.36	100.89	177.856 ± 6.448	94.272 ± 23.013
191004B	894718	3.503	18.816 ± 7.008	5.712 ± 0.279	31.09	77.73	15.626 ± 3.17	5.232 ± 0.357
191011A	883832	1.722	372.32 ± 13.76	55.136 ± 1.552	51.43	128.58	193.312 ± 13.36	17.648 ± 0.426
200205B	954520	1.465	116.56 ± 2.732	53.056 ± 2.838	56.8	141.99	114.304 ± 5.166	40.016 ± 13.073
200829A	993768	1.25	64.416 ± 17.16	2.848 ± 0.057	62.22	155.56	6.352 ± 0.283	2.192 ± 0.057
201020A	1000926	2.903	14.17 ± 2.945	3.728 ± 1.859	35.87	89.67	7.216 ± 0.893	3.264 ± 0.708
201021C	1001130	1.07	21.584 ± 3.301	8.528 ± 2.132	67.63	169.08	9.136 ± 2.172	4.16 ± 2.515
201104B	1004168	1.954	10.448 ± 2.883	5.552 ± 0.417	47.39	118.48	8.56 ± 0.23	5.104 ± 0.486

-
- [1] F.-W. Zhang, Y.-Z. Fan, L. Shao, and D.-M. Wei, *Astrophys. J. Lett.* **778**, L11 (2013), 1309.5612.
- [2] P. Kumar and B. Zhang, *Physics Reports* **561**, 1 (2015), 1410.0679.
- [3] C. Kouveliotou, C. A. Meegan, G. J. Fishman, N. P. Bhat, M. S. Briggs, T. M. Koshut, W. S. Paciesas, and G. N. Pendleton, *Astrophys. J. Lett.* **413**, L101 (1993).
- [4] A. Levan, P. Crowther, R. de Grijs, N. Langer, D. Xu, and S.-C. Yoon, *Space Science Reviews* **202**, 33 (2016), 1611.03091.
- [5] T. Piran, *Reviews of Modern Physics* **76**, 1143 (2004), astro-ph/0405503.
- [6] E. Nakar, *Physics Reports* **442**, 166 (2007), astro-ph/0701748.
- [7] E. Berger, *Ann. Rev. Astron. Astrophys.* **52**, 43 (2014), 1311.2603.
- [8] I. Horváth, *Astrophys. J.* **508**, 757 (1998), astro-ph/9803077.
- [9] I. Horváth, *Astron. & Astrophys.* **392**, 791 (2002), astro-ph/0205004.
- [10] I. Horváth, L. G. Balázs, Z. Bagoly, F. Ryde, and A. Mészáros, *Astron. & Astrophys.* **447**, 23 (2006), astro-ph/0509909.
- [11] I. Horváth, L. G. Balázs, Z. Bagoly, and P. Veres, *Astron. & Astrophys.* **489**, L1 (2008), 0808.1067.
- [12] B. Zhang, B.-B. Zhang, F. J. Virgili, E.-W. Liang, D. A. Kann, X.-F. Wu, D. Proga, H.-J. Lv, K. Toma, P. Mészáros, et al., *Astrophys. J.* **703**, 1696 (2009), 0902.2419.
- [13] I. Horváth, Z. Bagoly, L. G. Balázs, A. de Ugarte Postigo, P. Veres, and A. Mészáros, *Astrophys. J.* **713**, 552 (2010), 1003.0632.
- [14] O. Bromberg, E. Nakar, T. Piran, and R. Sari, *Astrophys. J.* **764**, 179 (2013), 1210.0068.
- [15] S. Kulkarni and S. Desai, *Astrophys. and Space Science* **362**, 70 (2017), 1612.08235.
- [16] M. Tarnopolski, *Astrophys. J.* **887**, 97 (2019), 1910.08968.
- [17] I. Horváth, B. G. Tóth, J. Hakkila, L. V. Tóth, L. G. Balázs, I. I. Rácz, S. Pintér, and Z. Bagoly, *Astrophys. and Space Science* **363**, 53 (2018), 1710.11509.

- [18] B. P. Abbott et al. (LIGO Scientific, Virgo, Fermi-GBM, INTEGRAL), *Astrophys. J. Lett.* **848**, L13 (2017), 1710.05834.
- [19] S. Boran, S. Desai, E. O. Kahya, and R. P. Woodard, *Phys. Rev. D* **97**, 041501 (2018), 1710.06168.
- [20] R. W. Klebesadel, I. B. Strong, and R. A. Olson, *Astrophys. J. Lett.* **182**, L85 (1973).
- [21] B. Paczynski, *PASP* **107**, 1167 (1995), astro-ph/9505096.
- [22] D. Q. Lamb, *PASP* **107**, 1152 (1995).
- [23] J. van Paradijs, P. J. Groot, T. Galama, C. Kouveliotou, R. G. Strom, J. Telting, R. G. M. Rutten, G. J. Fishman, C. A. Meegan, M. Pettini, et al., *Nature (London)* **386**, 686 (1997).
- [24] N. Gehrels, G. Chincarini, P. Giommi, K. O. Mason, J. A. Nousek, A. A. Wells, N. E. White, S. D. Barthelmy, D. N. Burrows, L. R. Cominsky, et al., *Astrophys. J.* **611**, 1005 (2004), astro-ph/0405233.
- [25] T. Piran, *Astrophys. J. Lett.* **389**, L45 (1992).
- [26] B. Paczynski, *Nature (London)* **355**, 521 (1992).
- [27] G. Goldhaber, D. E. Groom, A. Kim, G. Aldering, P. Astier, A. Conley, S. E. Deustua, R. Ellis, S. Fabbro, A. S. Fruchter, et al., *Astrophys. J.* **558**, 359 (2001), astro-ph/0104382.
- [28] M. R. S. Hawkins, *Mon. Not. R. Astron. Soc.* **405**, 1940 (2010), 1004.1824.
- [29] J. P. Norris, R. J. Nemiroff, J. D. Scargle, C. Kouveliotou, G. J. Fishman, C. A. Meegan, W. S. Paciesas, and J. T. Bonnell, *Astrophys. J.* **424**, 540 (1994), astro-ph/9312049.
- [30] H. Che, Y. Yang, M. Wu, and Q. B. Li, *Astrophys. J. Lett.* **483**, L25 (1997).
- [31] M. Deng and B. E. Schaefer, *Astrophys. J. Lett.* **502**, L109 (1998).
- [32] A. Lee, E. D. Bloom, and V. Petrosian, *Astrophys. J. Suppl. Ser.* **131**, 21 (2000), astro-ph/0002218.
- [33] H.-Y. Chang, *Astrophys. J. Lett.* **557**, L85 (2001), astro-ph/0106220.
- [34] T. Sakamoto, S. D. Barthelmy, W. H. Baumgartner, J. R. Cummings, E. E. Fenimore, N. Gehrels, H. A. Krimm, C. B. Markwardt, D. M. Palmer, A. M. Parsons, et al., *Astrophys. J. Suppl. Ser.* **195**, 2 (2011), 1104.4689.
- [35] D. Kocevski and V. Petrosian, *Astrophys. J.* **765**, 116 (2013).
- [36] D. Gruber, J. Greiner, A. von Kienlin, A. Rau, M. S. Briggs, V. Connaughton, A. Goldstein, A. J. van der Horst, M. Nardini, P. N. Bhat, et al., *Astron. & Astrophys.* **531**, A20 (2011), 1104.5495.
- [37] A. Lien, T. Sakamoto, S. D. Barthelmy, W. H. Baumgartner, J. K. Cannizzo, K. Chen, N. R. Collins, J. R. Cummings, N. Gehrels, H. A. Krimm, et al., *Astrophys. J.* **829**, 7 (2016), 1606.01956.
- [38] D. F. Crawford, arXiv e-prints arXiv:1804.10274 (2018), 1804.10274.
- [39] M. Tarnopolski, *Astrophys. J.* **897**, 77 (2020), 2004.13623.
- [40] V. Z. Golkhou and N. R. Butler, *Astrophys. J.* **787**, 90 (2014), 1403.4254.
- [41] K. Gopika and S. Desai, *Physics of the Dark Universe* **30**, 100707 (2020), 2006.12320.
- [42] S. Pradyumna, S. Gupta, S. Seeram, and S. Desai, *Physics of the Dark Universe* **31**, 100765 (2021), 2011.06421.
- [43] K. Bora and S. Desai, *JCAP* **2021**, 012 (2021), 2008.10541.
- [44] Y. Tian, K. Umetsu, C.-M. Ko, M. Donahue, and I. N. Chiu, *Astrophys. J.* **896**, 70 (2020), 2001.08340.
- [45] D. Foreman-Mackey, D. W. Hogg, D. Lang, and J. Goodman, *Publications of the Astronomical Society of the Pacific* **125**, 306 (2013).
- [46] A. Pélangeon, J. L. Atteia, Y. E. Nakagawa, K. Hurley, A. Yoshida, R. Vanderspek, M. Suzuki, N. Kawai, G. Pizzichini, M. Boër, et al., *Astron. & Astrophys.* **491**, 157 (2008), 0811.3304.
- [47] S. D. Barthelmy, L. M. Barbier, J. R. Cummings, E. E. Fenimore, N. Gehrels, D. Hullinger, H. A. Krimm, C. B. Markwardt, D. M. Palmer, A. Parsons, et al., *Space Science Reviews* **120**, 143 (2005), astro-ph/0507410.
- [48] O. M. Littlejohns, N. R. Tanvir, R. Willingale, P. A. Evans, P. T. O'Brien, and A. J. Levan, *Mon. Not. R. Astron. Soc.* **436**, 3640 (2013), 1309.7045.
- [49] A. von Kienlin, C. A. Meegan, W. S. Paciesas, P. N. Bhat, E. Bissaldi, M. S. Briggs, E. Burns, W. H. Cleveland, M. H. Gibby, M. M. Giles, et al., *Astrophys. J.* **893**, 46 (2020), 2002.11460.
- [50] C. Markwardt, S. Barthelmy, J. Cummings, D. Hullinger, H. Krimm, and A. Parsons, NASA/GSFC, Greenbelt, MD **6** (2007).
- [51] N. Swift Team, *Swift archive*, <https://swift.gsfc.nasa.gov/archive/> (2021).
- [52] NASA, *Xamin web interface*, <https://heasarc.gsfc.nasa.gov/xamin/> (2021).
- [53] NASA, *Web hera*, <https://hera.gsfc.nasa.gov/hera/> (2021).
- [54] J. D. Scargle, J. P. Norris, B. Jackson, and J. Chiang, arXiv e-prints arXiv:1304.2818 (2013), 1304.2818.